ISTANBUL TECHNICAL UNIVERSITY ★ GRADUATE SCHOOL

DESIGN AND FABRICATION OF MAGNETICALLY ACTUATED CELL SORTER

M.Sc. THESIS

Merve GÜLLE

Department of Electronics and Communication Engineering

Electronics Engineering Programme

JULY 2021

ISTANBUL TECHNICAL UNIVERSITY ★ GRADUATE SCHOOL

DESIGN AND FABRICATION OF MAGNETICALLY ACTUATED CELL SORTER

M.Sc. THESIS

Merve GÜLLE
(504181215)

Department of Electronics and Communication Engineering

Electronics Engineering Programme

Thesis Advisor: Assist. Prof. Ahmet Can ERTEN

JULY 2021

İSTANBUL TEKNİK ÜNİVERSİTESİ ★ LİSANSÜSTÜ EĞİTİM ENSTİTÜSÜ

MANYETİK OLARAK KONTROL EDİLEBİLEN HÜCRE SINIFLANDIRICI TASARIMI VE ÜRETİMİ

YÜKSEK LİSANS TEZİ

Merve GÜLLE
(504181215)

Elektronik ve Haberleşme Mühendisliği Anabilim Dalı

Elektronik Mühendisliği Programı

Tez Danışmanı: Dr. Öğr. Üyesi Ahmet Can ERTEN

TEMMUZ 2021

Merve GÜLLE, a M.Sc. student of ITU Graduate School student ID 504181215, successfully defended the thesis entitled "DESIGN AND FABRICATION OF MAGNETICALLY ACTUATED CELL SORTER", which she prepared after fulfilling the requirements specified in the associated legislations, before the jury whose signatures are below.

Thesis Advisor :	**Assist. Prof. Ahmet Can ERTEN** İstanbul Technical University	.....
Jury Members :	**Assoc. Prof. Onur FERHANOĞLU** İstanbul Technical University	.....
	Prof. Dr. Alper KİRAZ Koç University	.....

Date of Submission : 11 June 2021
Date of Defense : 1 July 2021

FOREWORD

I would like to extend my deepest appreciation to my academic advisor Assist. Prof. Ahmet Can Erten for his valuable guidance, and support. I would like to thank him for giving me the opportunity to participate in this interesting research, giving me chance to work in his Electro-Optical Devices Laboratory (EDL) where I conducted my thesis project under his guidance and helping me improve my academic skills. I would like to thank Prof. Dr. Alper Kiraz from Koç University for giving me the opportunity to work in his Opto-fluidics and Nano-optics Research Laboratory. I would like to thank Assist. Prof. Onur Ferhanoğlu for his supportive advice, and motivation during my work. In addition, I would like to thank Oğuz Gürcüoğlu, İsraa Salaheldin, and other EDL members for their support.

Finally, special thanks to Istanbul Technical University Research Fund BAP for supporting this work under project no 42524.

June 2021

Merve GÜLLE
Electronics Engineer

TABLE OF CONTENTS

Page

ABBREVIATIONS

FACS	**:** Fluorescence-activated Cell Sorting
MACS	**:** Magnetic-activated Cell Sorting
DEP	**:** Dielectrophoresis
μFACS	**:** Micro Fluorescence-activated Cell Sorting
PZT	**:** Piezoelectric
TSAW	**:** Travelling Surface Acoustic Waves
PDMS	**:** Polydimethylsiloxane
CI	**:** Carbonyl Iron
CI-LA	**:** Lauric Acid Coated Carbonyl Iron
SPION-LA	**:** Lauric Acid Coated Superparamagnetic Iron-oxide
HMDS	**:** Hexamethyldisiloxane
PLA	**:** Poly Lactic Acid
TPU	**:** Thermoplastic Poly Urethane
2D	**:** 2-Dimensional
3D	**:** 3-Dimensional

SYMBOLS

$\mathbf{w_0}$	: Maximum deflection of the membrane
$\boldsymbol{\nu_M}$	: Poisson's ratio of the membrane
$\mathbf{E_M}$	: Young's modulus of the membrane
$\mathbf{d_M}$	: Thickness of the membrane
$\mathbf{D_M}$	: Diameter of the membrane
$\boldsymbol{\Delta p}$	: Pressure drop
$\boldsymbol{\mu_0}$	: Magnetic permeability of the free space
$\mathbf{B}$	: Magnetic flux density
$\mathbf{H}$	: Magnetic field
$\mathbf{M}$	: Magnetization
$\mathbf{M_n}$	: n. mold
$\mathbf{C_n}$	: n. chip
$\mathbf{R_H}$	: Hydraulic resistance
$\mathbf{P_0}$	: Pressure applied to membranes
$\mathbf{P_M}$	: Pressure of the chamber entrance
$\mathbf{v_0}$	: Flow velocity of main channel
$\mathbf{v_x}$	: Lateral flow velocity
$\mathbf{Q_x}$	: Lateral volumetric flow rate
$\mathbf{Q_{x0}}$	: Initial lateral volumetric flow rate
$\mathbf{W_C}$	: Width of the main channel
$\mathbf{W_M}$	: Width of the channel between main channel and membranes
$\mathbf{H_C}$	: Height of the main channel
$\mathbf{L_M}$	: Length of the channel between main channel and membranes
$\mathbf{t}$	: Time
$\boldsymbol{\tau}$	: Time constant
$\boldsymbol{\eta}$	: Liquid viscosity
$\boldsymbol{\Delta V_M}$	: Volume change in the chambers
$\boldsymbol{\Delta x}$	: Drift distance
$\boldsymbol{\Delta t}$	: Drift duration

LIST OF TABLES

Page

LIST OF FIGURES

Page

DESIGN AND FABRICATION OF MAGNETICALLY ACTUATED CELL SORTER

SUMMARY

Cell sorting is the process of isolating a target cell type from a complex biofluid based on its characteristics. This process has become a widely used method for various purposes such as basic biological research, and clinical diagnostics. Developing microfluidic technology has made it possible for cell sorters to work more efficiently with less sample fluids in much smaller sizes compared to conventional methods. Microfluidic lab-on-a-chip platforms enable low-cost, disposable, and lightweight instruments in which various elements, such as magnetic, optics, or acoustics, are strongly integrated on a single plastic chip to operate to develop unique features. PDMS (polydimethylsiloxane), on the other hand, has been a major factor in the development of microfluidic technology, as it is bio-compatible, transparent and low-cost. It has also become one of the most widely used basic materials in microfluidic cell sorters.

Microfluidic cell sorters can be examined under two headings as passive and active. Passive sorters classify cells according to their physical properties such as size and density, using the channel geometry and hydrodynamic structure of the chip. They can operate at high speed and do not require an external power source, but fail to separate cells with similar physical properties. In such cases, cells need to be labeled and classified by active cell sorters. Active cell sorters are divided into four main categories: fluorescence-activated cell sorting (FACS), magnetic-activated cell sorting (MACS), dielectrophoresis (DEP) and acoustic microsystems. Fluorescence-activated microfluidic cell sorters (μFACS) are the most preferred cell sorter type by biomedical researchers and clinicians due to their high sensitivity and efficiency.

A μFACS systems perform the separation process by detecting the fluorescence emitted by cells with the help of a camera system and then directing the cells to the relevant outlet. Cell manipulation can be done with various structures such as piezoelectric actuators, surface acoustic waves, optical triggers. However, these methods have the disadvantages of having large dimensions, requiring complex production steps and operating at low efficiency, respectively.

Magnetic membranes are widely used in microfluidic systems due to their high elasticity, low response time and no need for on-chip power supply. Due to their wide deflection range, ease of fabrication, low power consumption, small size and low response time, they are very good candidates for use as actuators in μFACS systems. In this study, a μFACS system has magnetic membrane actuators was proposed, designed, simulated, mathematically modeled, manufactured and tested.

Magnetic membranes were obtained by incorporating CI (carbonyl iron) microparticles into PDMS polymer. The CI-PDMS mixture was spread on the kapton tape with spin coating and cured in oven. After fabrication, the cross-section of the magnetic

membranes was examined with a microscope and a quite homogeneous structure without agglomeration with a thickness of 30 μm was observed. The fabricated membranes were assembled with PDMS structures with oxygen plasma bonding. The deflection amounts of the membranes applied magnetic field with neodymium (NdFeB) permanent magnets were measured. The maximum deflection was recorded as 597 μm from the 6.83 mm diameter membrane and the 4 mm diameter magnet. In addition, the deflection experiments were simulated with COMSOL Multiphysics. Membranes were defined as hyperelastic materials with relative magnetic permeability greater than 1. The elastic modulus of the membrane which is unknown was accepted as equal to that of PDMS, and the relative magnetic permeability was set by inverse modeling by taking some of the experimental results. As a result, the established simulation scheme could manage to show consistency with the experimental results with a value of R^2 over 0.95.

The microfluidic cell sorter, on the other hand, consists of three basic parts: glass base, PDMS body and magnetic membrane. The PDMS body has a micro channels pattern on its surface. The mold produced with kapton tape was used to create the micro channels. The channel pattern drawn in 2D was transferred to kapton tape with an electronic craft cutter (Silhouette). Then, liquid PDMS was poured on the molds and hardened in the oven to obtain the PDMS bodies containing micro channels. With this technique, which is not yet available in the literature, the mold production phase has been made quite practical without the need for any chemical processing. The electronic craft cutter was able to cut kapton tape with an error of less than 10% for sizes 500 μm and above. However, it was not successful enough in cutting sharp corners. In addition, the molds need to be renewed as they deform after a few uses. Chip fabrication was continued with the PDMS body by punching holes for inlets, outlets, and membrane chambers. In the last step, microscope lame, PDMS body, and magnetic membrane were assembled with oxygen plasma bonding. Thus, cell sorter chips with dimensions of 75 mm x 25 mm x 5 mm were obtained, which took 5-6 hours to manufacture. In order to examine the effect of different dimensions on the channel geometry, chips with channels of four different sizes were produced.

In addition, an electrically controllable magnetic actuator containing permanent magnets was fabricated to actuate the magnetic membranes. A body with PLA (poly lactic acid) filament and an oscillating spring structure to which permanent magnets are attached with TPU (thermoplastic polyurethane) flexible filament were produced by 3D printer. Two inductors are used just below the magnets. And finally, inductors, body, spring structure and magnets are assembled with epoxy. The magnets were enabled to oscillate with a magnetic field which is created by applying a voltage to the inductors. A structure that can apply electrically controlled magnetic force to the membranes was provided by aligning the magnetic actuator directly under the membranes. Thus, electrically controllable magnetic actuators that can operate with a voltage of 10 V and below, could be produced.

In addition, the cell sorter chip was mathematically modeled in order to find the optimum chip geometry and to calculate the chip performance theoretically. The model is based on fundamental fluid mechanics. With this model, it was concluded that the chip size should be as small as possible and the liquid flow rate should be high in order to improve the chip performance. In this study, the lower limit of the channel widths

was determined by the resolution of the electronic paper cutter and the narrowest main channel could be produced as 750 μm.

The chips were simulated with the COMSOL Multiphysics. For the simplicity of the model, only the cell manipulation area of the chips was studied by simulation. Membranes, bio-fluid, and the cells were modeled with the Solid Mechanics, Laminar Flow, and Particle Tracing for Fluid Flow modules respectively. The simulation results were compatible with the mathematical model and experiments.

Finally, the chips were tested. In the tests, the sample fluid was represented by water dyed with food coloring, and the buffer liquid was represented by plain water. Experiments were carried out by varying the amplitude of the applied voltage, pulse width and inflow velocity for the chips with different channel sizes. Experimental results were compatible with theoretical calculations and simulation results. However, when the experiments were repeated under the same conditions, the exact same results could not be obtained. This is thought to be due to the large size of the channels and the difficulty of setting the membranes completely flat in their initial state.

As a result, in this study, it has been achieved to produce a microfluidic cell sorter that can operate with 8 V voltage, have a throughput of 10 cells/s. The outputs of the chips could not be observed, as the outputs could not be cut properly enough with the electronic craft cutter. Only the deviation of the dyed water in the cell manipulation area could be observed. With this study, it has been shown that microfluidic cell sorters can be operated with magnetic membrane actuators. Practical and innovative fabrication techniques such as electronic paper cutter, 3D printer have been proposed and applied. Unfortunately, a very low throughput has been achieved compared to other cell sorters in the literature. With the theoretical calculations and simulation results, it has been shown that this cell sorter, which can be controlled by magnetic membranes could rival those in the literature by fabricating in smaller sizes with advanced techniques.

MANYETİK OLARAK KONTROL EDİLEBİLEN HÜCRE SINIFLANDIRICI TASARIMI VE ÜRETİMİ

ÖZET

Hücre sınıflandırma, çeşitli hücre türlerinin bulunduğu biyolojik bir sıvının içerisinden belirli bir hücre tipinin ayrıştırılması işlemidir. Bu işlem temel biyolojik araştırmalar, klinik teşhisler gibi birçok amaçla yaygın olarak kullanılmaktadır. Gelişen mikroakışkan teknolojisi hücre sınıflandırıcıların gelenkesel yöntemlere göre çok daha küçük boyutlarda, az örnek sıvılarıyla daha verimli bir şekilde çalışmalarını olanaklı kılmıştır. Manyetik, optik, akustik v.b. yapılarla entegre olabilen mikroakışkan çipler ile çeşitli fonksiyonları bünyesinde birleştirebilen, tek kullanımlık, düşük maliyetli çipler üretmek mümkündür. PDMS (polydimethylsiloxane) ise biyouyumlu, saydam ve ucuz olması sebebiyle mikroakışkan teknolojisinin gelişmesinde oldukça büyük bir faktör olmuştur. Ayrıca mikroakışkan hücre sınıflandırıcılarında en yaygın kullanılan temel malzemelerden bir haline gelmiştir.

Mikroakışkan hücre sınıflandırıcılar pasif ve aktif olmak üzere iki başlıkta incelenebilir. Pasif sınıflandırıcılar hücreleri boyut, yoğunluk gibi sahip oldukları fiziksel özelliklere göre çipin kanal geometrisi ve hidrodinamik yapısından faydalanarak sınıflandırırlar. Yüksek hızda çalışabilirler ve harici bir güç kaynağına ihtiyaç duymazlar fakat benzer fiziksel özelliklere sahip hücreleri ayrıştırmakta başarısızdırlar. Böyle durumlarda hücrelerin etiketlenmesi ve aktif hücre sınıflandırıcıları ile sınıflandırılması gerekmektedir. Aktif hücre sınıflandırıcılar floresanla aktive olan sınıflandırıcılar (FACS), manyetik aktif hücre sınıflandırıcılar (MACS), dielektroforez (DEP) ve akustik mikrosistemler olmak üzere dört ana başlığa ayrılırlar. Floresanlar aktive olan mikroakışkan hücre sınıflandırıcılar (μFACS) yüksek hassasiyeti ve verimi sebebiyle biyomedikal araştırmacılar ve klinisyenler tarafından en çok tercih edilen hücre sınıflandırıcı tipidir.

Bir μFACS sistem hücrelerin yaydığı floresanı bir kamera sistemi yardımıyla tespit eder ve hücreleri ilgili olduğu çıkışa yönlendirerek ayrıştırma işlemini uygular. Hücre yönlendrime işlemi ise piezoelektrik aktüatörler, yüzey akustik dalgalar, optik tetikleyicler gibi çeşitli yapılarla yapılabilir. Fakat bu yöntemlerin sırasıyla büyük boyutlara sahip olma, karmaşık üretim aşamaları gerektirme ve düşük verimde çalışmak dezavantajları vardır.

Manyetik membranlar yüksek elastisitesi, düşük tepki süresi ve çip üzerinde güç kaynağına ihtiyaç duymaması olması sebebiyle mikroakışkan sistemlerde oldukça yaygın bir kullanıma sahiptir. Yüsek sapma miktarı, üretim kolaylığı, düşük güç tüketimi, küçük boyutlarda olması ve düşük tepki süresi sebebiyle μFACS sistemlerde aktüatör olarak kullanılmak için oldukça iyi adaylardır. Bu çalışma ise hücre yönlendirici aktüatör olarak manyetik membran kullanan bir μFACS sistem önerilmiş, tasarlanmış, benzetimleri yapılmış, matematiksel olarak modellenmiş, üretilmiş ve test edilmiştir.

Manyetik membranlar CI (karbonil demir) mikroparçacıkları ile PDMS polimerinin karıştırılması ile elde edilmiştir. Hazırlanan karışım kapton bant üzerine spin kaplama ile yayılmış ve son olarak fırınlanarak sertleşmesi sağlanmıştır. Yanal kesiti mikroskop ile incelenen membranlarda manyetik parçacıkların topaklanması gözlenmemiştir ve 30 μm kalınlığında oldukça homojen bir yapı elde edilmiştir. Üretilen membranlar oksijen plasma yapıştırma cihazı ile PDMS gövdelerle birleştirilmiştir. Neodimyum (NdFeB) kalıcı magnetlerle manyatik alan uygulanan membranların sapma miktarları ölçülmüştür. Maksimum sapma 6.83 mm çaplı membran ve 4 mm çaplı magnetten 597 μm olarak ölçülmüştür. Ayrıca sapma deneylerinin COMSOL Multiphysics uygulaması ile benzetimleri yapılmıştır. Membranlar göreli manyetik geçirgenliği 1'den büyük olan hiperelastik malzeme olarak tanımlanmıştır. Membranların bilinmeyen parametrelerinden elastik modülü PDMS'inkiyle eşit kabul edilmiş, göreli manyetik geçirgenliği ise yapılan deney sonuçlarının bazıları alınarak ters modelleme ile en uygun değer seçilmiştir. Sonuç olarak kurulan benzetim şeması deney sonuçları ile 0.95'in üzerinde bir R^2 değeriyle örtüşmeyi başarmıştır.

Mikroakışkan hücre sınıflandırıcı ise cam taban, PDMS gövde ve manyetik membran olmak üzere üç temel kısımdan oluşmaktadır. PDMS gövdenin cam taban ile birleştiği tarafında mikro kanallar bulunmaktadır. Mikro kanalların oluşturulması için kapton bant ile üretilen kalıp kullanılmıştır. 2 boyutlu olarak çizilen kanal deseni elektronik kağıt kesici (Silhouette) ile kapton banda aktarılmıştır ve üzerine sıvı PDMS dökülüp fırında sertleştirilerek mikronkanallar içeren PDMS gövde elde edilmiştir. Literatürde henüz bulunmayan bu teknik ile kalıp üretimi aşaması herhangi bir kimyasal işleme gerek duymayarak oldukça pratikleştirilmiştir. Elektronik kağıt kesici 500 μm ve üzeri boyutlar için 10%'un altında hata ile kapton bandı kesmeyi başarabilmiştir. Fakat keskin köşelerin kesilmesinde yeterince başarılı olamamıştır. Ayrıca kalıplar birkaç kullanımdan sonra deforme oldukları için yenilenmeye ihtiyaçları vardır. Çip üretimi PDMS gövdeye girişler, çıkışlar ve membran hazneleri için delik açılması ile devam eder. Son aşamda ise mikroskop lamı, PDMS gövdeve manyetik membran oksijen plazma yapıştırma cihazı ile birleştirilmiştir. Böylece üretimi 5-6 saat civarı süren, 75 mm x 25 mm x 5 mm boyutlarında hücre sınıflandırıcı çipler elde edilmiştir. Kanal geometrisindeki farklı boyutların etkisini inceleyebilmek için dört farklı boyutlarda kanallara sahip çipler üretilmiştir.

Ayrıca manyetik membranları çalıştırmak için kalıcı magnet içeren, elektrik olarak kontrol edilebilen manyetik aktüatörler üretilmiştir. 3 boyutlu yazıcı ile PLA (polilaktik asit) filamenti ile gövde, TPU (termoplastik poliüretan) esnek filamenti ile kalıcı magnetlerin tutturulduğu salınabilen yaylı bir yapı üretilmiştir. Magnetlerin hemen altına gelecek şekilde iki adet indüktör kullanılmıştır. Ve son olarak indüktörler, gövde, yaylı yapı ve magnetler epoksi ile yapıştırılmıştır. İndüktörlere uygulanan gerilim ile magnetlerin üzerinde manyetik alan oluşturularak magnetlerin salınması sağlanmıştır. Manyetik aktüatör, magnetler membranların tam altına gelecek şekilde yerleştirilerek membranlara elektriksel kontrollü manyetik kuvvet uygulayabilen bir yapı sağlanmıştır. Böylece 10 V ve altında çalıştırabilen, kolay üretilebilir, düşük güç tüketen, elektriksel olarak kontrol edilebilen manyetik aktüatörler üretilmişir.

Ayrıca optimum çip geometrisini bulabilmek ve çip performansını teorik olarak hesaplayabilmek için hücre sınıflandırıcı çipin matematiksel modellemesi yapılmıştır. Model temel akışkanlar mekaniğine dayandırılarak yapılmıştır. Bu model ile çip performansının iyileştirilebilmesi için çip boyutlarının mümkün olduğunca küçük, sıvı

akış hızının ise yüksek olması gerektiği sonucuna varılmıştır. Bu çalışmada ise kanal genişleiklerinin alt sınırını elektronik kağıt kesicinin çözünürlüğü belirlemiştir ve en dar ana kanal 750 μm olarak üretilebilmiştir.

Çiplerin COMSOL Multiphysics uygulaması ile benzetimleri de yapılmıştır. Modelin basitliği bakımından çiplerin yalnızca hücre yönlendirme bölümü benzetimle incelenmiştir. Katı Mekaniği modülü ile membranlar, Doğrusal Akış modülü ile biyolojik sıvı, Akışkanlar için Parçacık Takibi modülü ile hücreler modellenmiştir. Benzetim sonuçları matematiksel modelle ve deneylerler uyumlu çıkmıştır.

Son olarak çipler test edilmiştir. Testlerde hücre sıvısı gıda boyası ile renklendirilmiş suyla, tampon sıvı ise sade suyla temsil edilmiştir. Farklı kanal boyutlarına sahip çipler ile uygulanan gerilimin genliği, darbe genişliği ve akış hızı değiştirilerek deneyler yapılmıştır. Deney sonuçları teoreik hesaplarla ve benzetim sonuçlarıyla uyumlu çıkmıştır. Fakat deneylar aynı şartlar altında tekrarlandığında birebir aynı sonuçlar alınamamıştır. Bunun kanal boyutlarının büyük olmasından ve membranların başlangıç durumunda tamamen düz olarak ayarlamanın zorluğundan kaynaklandığı düşünülmektedir.

Sonuç olarak bu çalışmada 10 hücre/s hızında 8 V gerilim ile çalışabilen bir mikroakışkan hücre sınıflandırıcı üretilmesi başarılmıştır. Çıkışlar elektronik kağıt kesici ile yeterince düzgün kesilemediğinden, çiplerin çıkışları gözlemlenememişir. Yalnızca hücre yönlendirme bölümündeki renki suyun sapması gözlemlenebilmiştir. Bu çalışma ile mikroakışkan hücre sınıflandırıcılarının manyetik membranlarla çalıştırılabileceği gösterilmiştir. Elektronik kağıt kesici, 3B yazıcı gibi pratik ve yenilikçi üretim teknikleri önerilmiş ve uygulanmıştır. Literatürdeki diğer hücre sınıflandırıcılara kıyasla oldukça düşük bir sınıflandırma hızına ulaşılabilinmiştir. Teorik hesaplamalarla ve benzetim sonuçları ile farklı üretim teknikleri ile daha küçük boyutlarla üretilmesi başarıldığında manyetik membranlarla kontrol edilebilen bu hücre sınıflanrıcı ile literatürdekilere rakip olabilecek performansta çiplerin üretilebilineceği gösterilmiştir.

1. INTRODUCTION

1.1 Overview

Cell sorting, in definition, refers to any procedure that isolates a target cell type from a complex biofluid based on its characteristics [1, 2]. Sorting of biological cells has become a widely used method for basic biology research, drug discovery, and clinical diagnosis, in which the enrichment of cells of interest from heterogeneous populations is a crucial step before the study [3–5]. For example, cell sorting is needed to count white blood cells, red blood cells, and platelets for assessing various blood disorders such as anemia, as well as other medical conditions that indirectly affect the blood such as infections [6]. Similarly, cell sorters can be a useful tool to analyze circulating tumor cells (CTC) in order to monitor disease progression [7].

1.2 Microfluidic Cell Sorters

Advancements in microfluidics have allowed the realization of miniaturized systems with capabilities that leverage a range of physical principles. Cell sorting on microchips offers various benefits over traditional approaches, including reduced equipment size, elimination of potentially biohazardous aerosols, and simplification of the complicated procedures typically associated with cell sorting [8]. Furthermore, microchip systems lend themselves well to parallelization, allowing for full lab-on-a-chip devices for cellular separation, research, and experimental processing. The lab-on-a-chip platform enables low-cost, disposable, and lightweight instruments in which several elements, such as magnetics [9], optics [10], or acoustics [11], are strongly integrated on a single plastic chip to operate to build innovative functionalities that would not have been feasible in traditional ways. Polydimethylsiloxane (PDMS) plays a great role in these advancements of microfluidic systems due to its many advantageous properties for prototyping: the material is cheap, optically transparent (transparency to visible light making it compliant with optical detection systems), and

bio-compatible; its moulding process is stable and simple to learn; and its simplicity enables the incorporation of elastomeric actuators and optical components [12–14].

1.2.1 Performance metrics for microfluidic cell sorters

Different sorting and separating methods have different capacities, which can result in output trade-offs with different applications. Therefore, it is important to have well-defined performance parameters to compare various strategies and the trade-offs between performance over the several sorting techniques. Here is the definitions of performance metrics for microfluidic single cell sorters based on the discussion in the book by Lee et al. [15]:

Purity is calculated by dividing the number of target cells by the total number of sorted cells (1.1). This shows the separation efficiency. Purity would be poor if the sorted cell population includes undesirable cells.

$$purity = \frac{\#\,of\ target\ cells}{\#\,of\ total\ sorted\ cells} \tag{1.1}$$

Yield is the ratio of the number of target cells collected to the number of target cells in the original sample (1.2). In some cases, target cells in the original sample may be lost due to lysis, adhesion to device surfaces, and retention within the device or tubing, therefore this term is used to express the proportion of the initial cells left in all outlets.

$$yield = \frac{\#\,of\ target\ cells\ collected}{\#\,of\ target\ cells\ in\ the\ original\ sample} \tag{1.2}$$

Enrichment is defined as the ratio of the number of target cells at the inlet divided by the total number of cells and the number of target cells at the outlet divided by the total number of cells (1.3). In other words, the term ‘enrichment’ refers to how much the concentration of target cells is enriched from inlet to outlet.

$$enrichment = \frac{\#\,of\ target\ cells\ at\ the\ inlet\ /\ \#\,of\ total\ cells\ at\ the\ inlet}{\#\,of\ target\ cells\ at\ the\ outlet\ /\ \#\,of\ total\ cells\ at\ the\ oulet} \tag{1.3}$$

Efficiency can be defined as the ratio between the number of sorted target cells and the number of target cells determined to sort (1.4). Cell sorting efficiency can be described when detection and sorting are separate processes.

$$efficiency = \frac{\#\,of\ target\ cells\ sorted}{\#\,of\ target\ cells\ identified\ to\ sort} \tag{1.4}$$

Throughput is reported as the number of cells sorted per time (1.5). This term refers to the measure of the sorting process.

$$throughput = \frac{\#\,of\,total\,sorted\,cells}{time} \tag{1.5}$$

1.2.2 Microfluidic cell sorter types

Microfluidic cell sorters can be divided into two categories as active and passive according to their separation method. While passive techniques rely entirely on channel geometry and endogenous hydrodynamic forces, active techniques depend entirely on an external force field for functionality [16].

Passive devices sort biological single cells according to their physical properties such as size [17], deformability [18], density [19] by utilizing channel geometry or intrinsic hydrodynamic phenomena such as inertial [20], pinched flow fractionation (PFF) [21], deterministic lateral displacement (DLD) [22], hydrophoresis [23]. Passive devices do not require external power devices, have simple structures, and have high throughput up to cells per second. On the other hand, passive microfluidic platforms can not distinguish the cells with similar physical properties. In such cases, cells need to be labeled so as to be distinguished and sorted by active cell sorters.

Active microfluidic cell sorters can be examined under four categories according to the labeling type of the cells as fluorescence-activated cell sorting (FACS) [24], magnetic-activated cell sorting (MACS) [9, 25], dielectrophoresis (DEP) [26], and acoustic microsystems [11, 27]. Active techniques can precisely monitor and modify cells of interest in real time, but their flow rate and resulting throughput are sluggish due to the long residual time required to expose cells to a physical field for effective sorting [28].

1.3 Micro-FACS (μFACS) Systems

A μFACS device in general consists of three main components; flow focusing, fluorescence detection, and cell manipulation (Figure 1.1). Flow focusing is accomplished with the help of a buffer solution. The buffer solution squeezes cells from the sample inlet into the main channel's middle line. Then, aligned cells are

identified as collection or waste with fluorescence detection. Finally, cells are oriented to the right outlet with an external force.

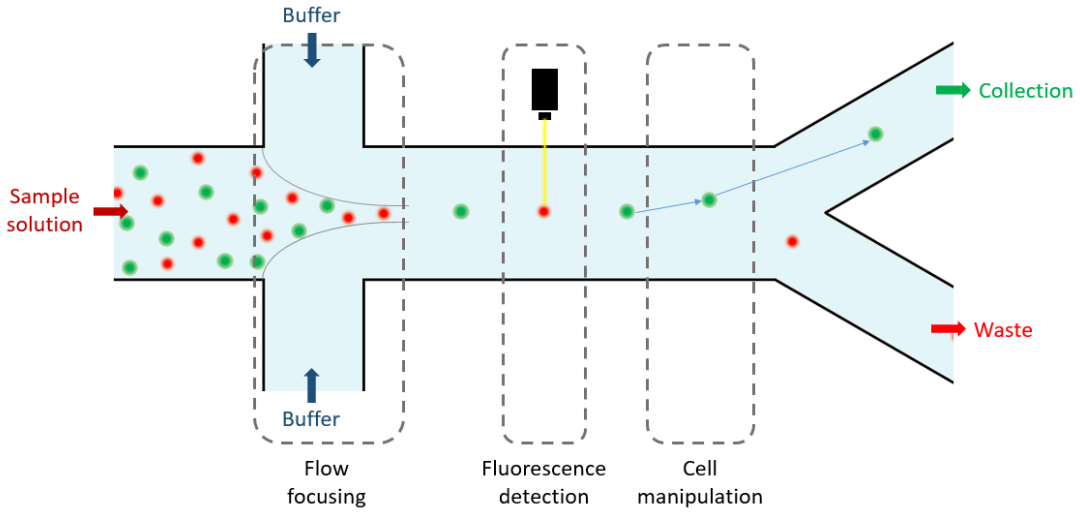

Figure 1.1 : A simplified schematic diagram for a typical μFACS device.

FACS devices distinguish a specific population of cells from a heterogeneous mixture dependent on each cell's fluorescence and light scattering properties. There are a variety of ways to mark cells, but for FACS research, antibodies labeled with fluorescent molecules, fluorescent proteins, and fluorescent nanoparticles were the most often used [29]. Bhagat et. al. calls FACS systems as the "Gold Standard", and according to him FACS devices have become the most preferred cell sorting approach among the biomedical researchers and clinicians because of their high sensitivity and throughput [16]. Commercial cell sorting systems have detectors that can detect between 14 and 17 separate fluorescent labels and can count/sort more than 100,000 cells per second [30]. As a result, they can simultaneously monitor and sort several fluorescent cell surface markers or fluorescent protein-tagged biomolecules.

1.3.1 Sorting mechanisms for μFACS devices

There are a variety of sorting mechanisms which are the most important part determining the working performance of cell sorters. The most widespread one among them is piezoelectric (PZT) actuators. Cheng et al. (2017) have been developed a μFACS device with PZT actuators which manipulating the flow laterally by applying a pulsed signal, and they could achieve a high throughput (1250 cells/s), and high purity (98%) [24]. Cai et al. (2020) have been implemented a new design by using PZT

actuators as microvalves at the outlets, and they achieved a high throughput (1800 cells/s), and high purity (>90%) [31]. Although the systems with PZT actuators are cost-effective, and have high sorting performances, the drawbacks of these systems are their bulky structures and fabrication difficulties.

Travelling surface acoustic waves (TSAW) are another actuation mechanism which are commonly used for sorting. In the cell manipulation region, cells are dragged with the TSAW [11, 32]. Such systems can work with high throughput and high purity performances, on the other hand they are disadvantageous as they need piezoelectric transducers and complicated fabrication processes.

Last but not least, cells can be sorted with optical trigger [33, 34]. For example, Meineke et al. (2016) have been improved a μFACS device which manipulates the flow by reducing the local viscosity via absorption of laser radiation [34]. As opposed to other micromanipulation methods, optical manipulation is typically the most versatile and adaptable since the manipulators can be reconfigured by changing the optical pattern. Optical manipulation, on the other hand, is less desirable because it has a lower throughput (tens of cells per second) and involves costly and complex devices [15].

1.3.1.1 Magnetic elastomer membrane actuators as a sorting mechanism

Considering all these reviews it is clear that there is a need for a sorting mechanism which can operate with high throughput and high purity sorting performances, is also easy to fabricate and has simple actuation mechanism.

Magnetic elastomer membrane actuators have been widely used in microfluidic applications [35–38] due to their broad deflection range provided by a low Young's modulus, high elasticity, rapid reaction to magnetic fields, an possible actuation without a power source on-chip [39, 40].

In this thesis "magnetic elastomer membrane actuators" are proposed as a sorting mechanism due to their large deflection range, easy fabrication, low power consumption, low chip area, and low response time. Then, a μFACS system works with magnetic membrane actuation is designed, simulated, mathematically modelled, and tested.

2. MAGNETIC MEMBRANE

2.1 Overview

Magnetic membranes are elastomer membranes that are incorporated magnetic material. They are flexible and deflected under magnetic field (Figure 2.1).

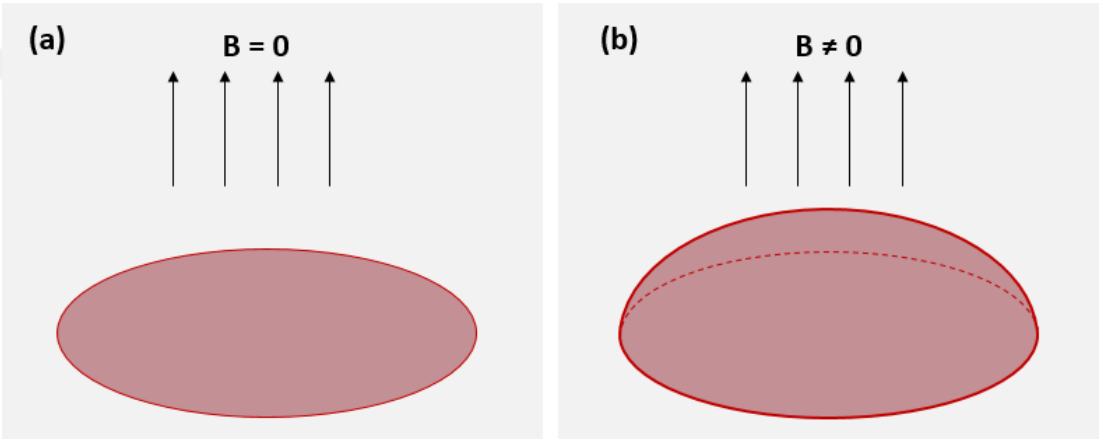

Figure 2.1 : Magnetic membrane a) flat condition, no magnetic field, b) deflection under magnetic field.

Magnetic membranes can produce a large deflection with low power consumption and low response time. Therefore, they are proposed as an effective actuation mechanism for micro-FACS systems in this thesis.

In our proposal device, two circular magnetic membranes placed on both sides of the main cell channel are deflected by magnetic field to change the flow pattern laterally and thus direct the cells to the intended outlets. The magnetic membranes are fabricated with polydimethylsiloxane (PDMS) and carbonyl iron (CI). As a result of our previous study, it is decided to use CI as magnetic particle since it is easily mixed with PDMS and it provides higher deflection compare to lauric acid coated superparamagnetic iron-oxide nanoparticles (SPION-LA) and lauric acid coated carbonyl iron microparticles (CI-LA) [41]. The actuation mechanism of

magnetic membranes is an electrically controllable, 3D printed platform that consists of NdFeB magnets and inductors.

2.2 Theoretical Analysis

According to Schomburg membranes can be investigated under two categories as thin and thick membranes based on the ratio of the maximum deflection amount and the thickness. If the maximum deflection is much less than the thickness, it is referred to as thick membrane; if it is greater than the thickness, it is referred to as thin membrane. Bending moments are dominant for thick membranes while the dominant force is stress due to straining for thin membranes [42].

In this thesis, magnetic membranes are fabricated as thin membranes due to intending large deflection with low force. Deflection of a circular thin membrane without residual stress due to Δp pressure drop is given in equation (2.1) [42].

$$w_0 = \left(\frac{3}{128} \frac{\left(1 - \nu_M^2\right)}{E_M} \frac{\Delta p}{d_M} \right)^{1/3} D_M^{4/3} \tag{2.1}$$

Here, E_M is Young's modulus, ν_M is Poisson's ratio, D_M is the diameter of the membrane, d_M is the thickness of the membrane, w_0 is the maximum deflection of the membrane.

2.3 Materials and Methods

2.3.1 Composite membrane fabrication

As the polymeric matrix, PDMS (RTV 615, Momentive) was obtained in the form of two components, a pre-polymer, and a cross-linker. As the magnetic particle, carbonyl iron (CI) powder ($\geq$ 97% Fe basis) is provided from Sigma-Aldrich. The diameter of the particles is observed as 2 μm with scanning electron microscopy analysis. According to Park, saturated magnetization, remnant magnetization, and coercivity of the particles are 175 emu/g, 20 emu/g, and 400 Oe respectively [43].

For magnetic membrane fabrication, first, 1 g PDMS pre-polymer and 0.4 g CI powder were stirred for about 5 minutes until no agglomeration was observed in the mixture. After that, 0.2 g of PDMS cross-linker was added to the mixture and stirred for 2

minutes. Then, the overall mixture was spin coated on a previously prepared kapton tape coated paper with a three step recipe: 500 rpm for 15 s, 1000 rpm for 15 s, and 2500 rpm for 30 s (Figure 2.2) [40]. Finally, spin coated magnetic membrane was baked overnight at 65 °C.

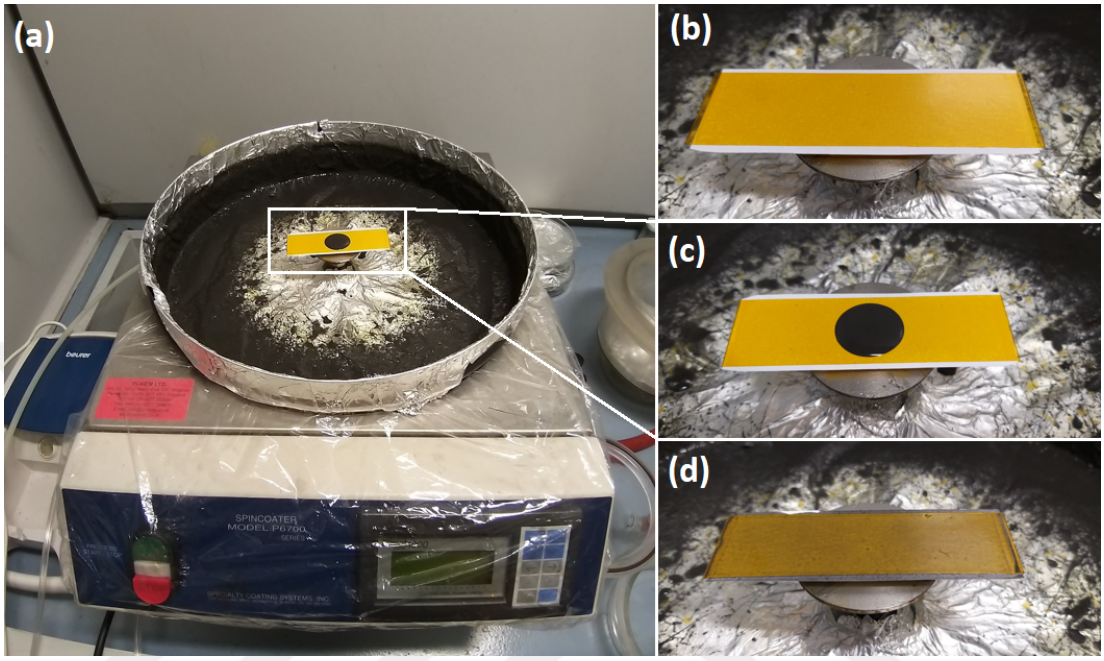

Figure 2.2 : Composite membrane fabrication. a) spin-coater, b) kapton tape coated paper, c) before spin coating, d) after spin coating.

2.3.2 Suspended circular membrane fabrication

As a magnetic membrane support platform, a PDMS chip with cylindrical hollows was manufactured. First, cylindrical structures with different diameters were produced for the mold by cutting plexiglass (Figure 2.3a). Then, the mold was kept in a closed container with Hexamethyldisiloxane (HMDS) overnight and its surface was silanized so that the PDMS structure could be easily removed from the mold. For the support structure, a PDMS mixture with the ratio of 5:1 (pre-polymer:cross-linker) was stirred thoroughly and degassed with a vacuum pump to get rid of the bubbles inside the mixture. Then, the mixture was poured over the mold and baked for 4 h at 65 °C. Next, the support structure was peeled off the mold (Figure 2.3b). After that, the support structure and magnetic membrane were bonded with oxygen plasma bonding (Figure 2.3c). Finally, the fabricated chips were punched at the bottom to ensure pressure balance in deflection experiments.

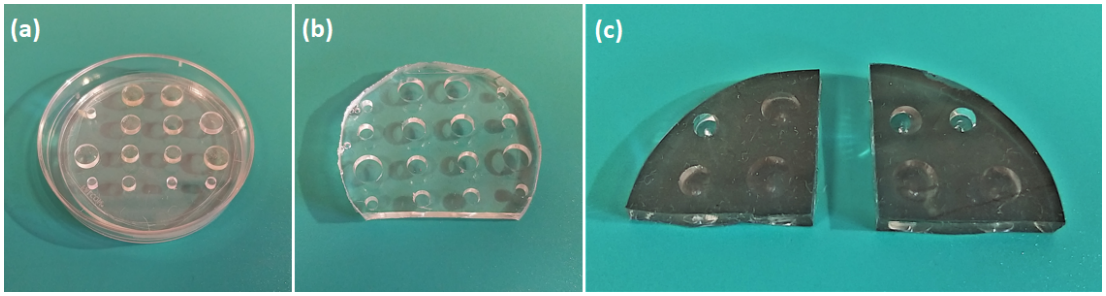

Figure 2.3 : Suspended circular membrane fabrication. a) Plexiglass mold, b) PDMS structure peeled off the mold, c)Magnetic membranes bonded to PDMS structure.

2.3.3 Measurement setup

In deflection experiments, circular magnetic membranes of 4 different diameters (3, 4, 5, 6 mm) were tested with rare earth (NdFeB) magnets of 2 different dimensions (3 and 4 mm of diameter and 1.5 and 2 mm of height respectively) by applying magnetic fields from different distances. The experiment setup is shown in Figure 2.4. The camera was set to focus on the deflection plane, and the summit of the membrane was illuminated with a laser pointer for a more clear picture. Magnetic membranes were recorded under the magnetic field, then, their deflections were measured with S-EYE computer software.

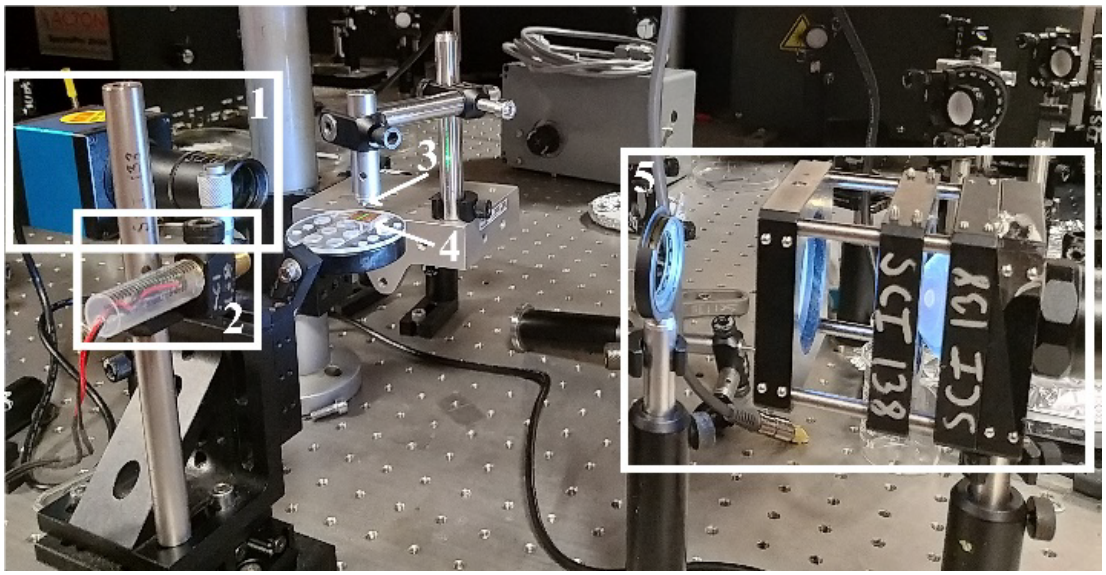

Figure 2.4 : Optical measurement setup: 1) camera, 2) laser pointer, 3) permanent magnet positioned directly above the membrane center, 4) magnetic membrane sample, 5) collimated light source.

An inverted microscope was used to determine the thickness of the membranes. Thin slices of chip cross-sections were cut out and optically imaged after the magnetic

membrane with support chip was released from the silicon wafer. The membrane thicknesses were measured using the reported cross-section images.

2.4 Simulation

In this thesis, COMSOL Multiphysics 5.2a was used as finite element analysis of the magnetic membranes by utilizing Solid Mechanics and Magnetic Field, No Currents modules. Owing to the radial symmetry of the environment, circular membrane and cylindrical magnet were drawn in 2D axisymmetric, as shown in Figure 2.5.

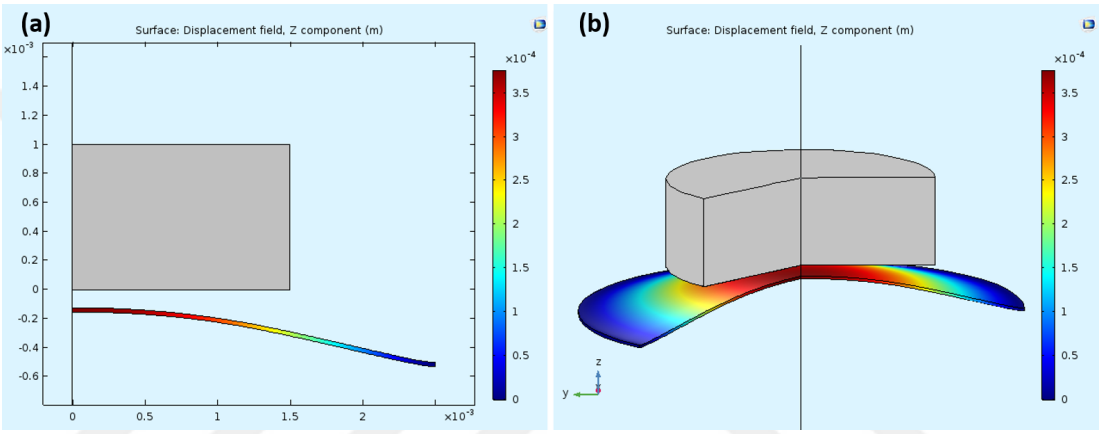

Figure 2.5 : a) 2D axisymmetry and b) 3D view of magnetic membrane deflected by a permanent magnet.

2.4.1 Modeling of permanent magnet

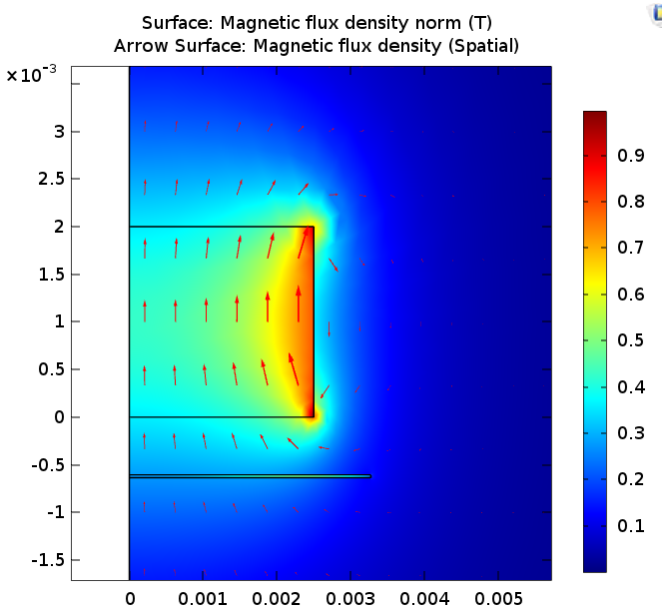

Figure 2.6 : Magnetic flux density [T] around the magnet in 2D axisymmetry.

According to magnetic constitutive law, the magnetic flux density (B) can be defined in terms of magnetic field (H) and magnetization (M) as in equation (2.2).

$$B = \mu_0 \left(H + M \right) \tag{2.2}$$

Here, μ_0 represents the magnetic permeability of the free space. A permanent magnet has a constant magnetization due to the nature of its material. Therefore, the permanent magnet was defined with Magnetic Flux Conservation in the Magnetic Field, No Current module. Magnetization is 915 kA/m for NdFeB magnets. The magnetic flux density and magnetic flux lines calculated by COMSOL Multiphysics are given in Figure 2.6.

2.4.2 Modeling of magnetic membrane

The magnetic membrane which consists of numerous magnetic microparticles and PDMS elastomer was defined as a single piece object to decrease the complexity of the simulation. The flexibility of PDMS was characterized by defining it as hyperelastic material in Solid Mechanics. In addition, by choosing its relative permeability of more than 1, the membrane was made affected by the magnetic field.

The key point is determining its lame parameter (μ) which is one-third of Young's modulus (E) for nearly incompressible materials and relative permeability (μ_r) to defining mechanic and magnetic properties of the membrane truly. The elastic modulus of pure PDMS has a 5:1 ratio is approximately 3.59 MPa [44]. However, according to Li, the CI particles have a strong interaction with the polymer network, so the stiffness of the CI-PDMS composite increases exponentially with the amount of CI [45]. In this thesis, the composite membrane has 25% weight ratio of CI to PDMS (5:1), and there is no study with the same values and materials in literature. Therefore, it was assumed that the composite membrane has the same elasticity as pure 5:1 PDMS, and its Young's modulus is 3.59 MPa.

Another key parameter for the membrane, relative permeability, was set as 1.85 depending on the maximum deflection values of the four different membranes under 2 different magnets.

2.5 Results

Using an inverted light microscope, the membrane thickness was measured as 30 μm for CI incorporated composite membrane (Figure 2.7). The membrane cross-section was observed to be quite homogeneous with the inverted light microscope.

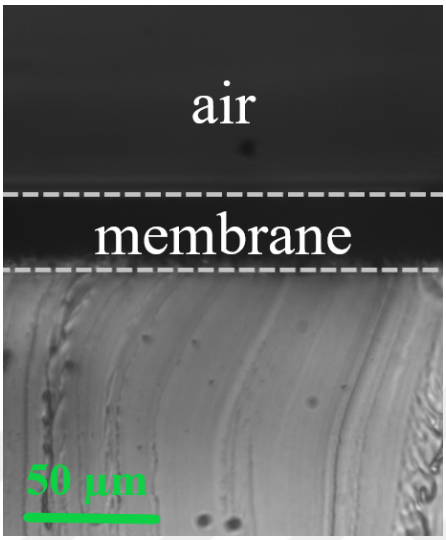

Figure 2.7 : Composite membrane-support chip assembly cross-section used for measuring membrane thickness profile. Thickness of the composite membrane was measured as 30 μm.

The final version of the magnetic membranes fabricated is given in Figure 2.8. In the beginning, it was intended to fabricate the membranes with diameters of 4, 5,6, and 7 mm. However, membrane diameters were measured as 3.77, 4.55, 5.73, and 6.83 mm respectively. The reason for this error comes probably from the cutting process of the plexiglass molds.

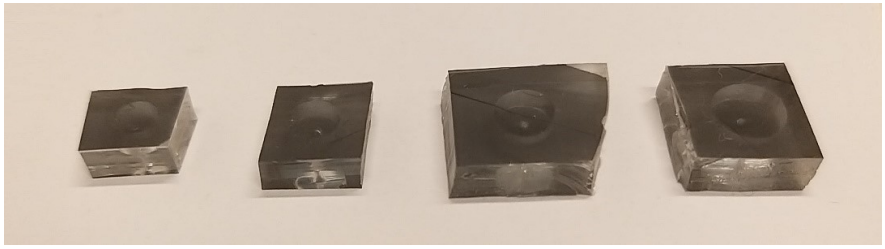

Figure 2.8 : Fabricated magnetic membrane chips. From left to right with the diameters of 3.77, 4.55, 5.73 and 6.83 mm.

Magnetic membranes with four different diameters (3.77, 4.55, 5.73, and 6.83 mm) were fabricated and deflected with NdFeB magnets (3 and 4 mm diameters and 1.5 and 2 mm height respectively) from different distances. Then, the deflection values were determined from the images taken by using edge detection in Matlab. The maximum

deflection was recorded as 597 μm from the membrane with 6.83 mm diameter and the magnet with 4 mm diameter and 2 mm height (Figure 2.9).

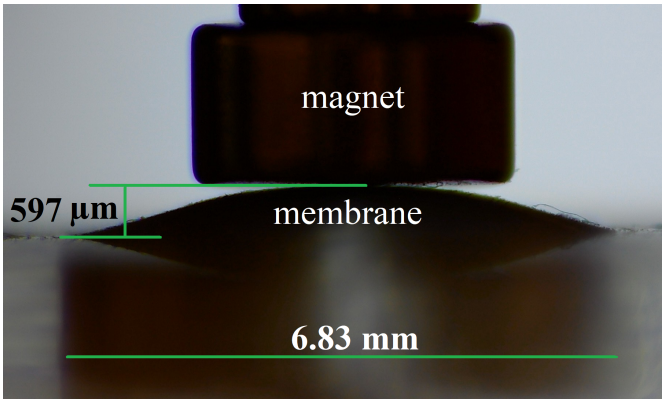

Figure 2.9 : Maximum deflection was measured as 597 μm.

Table 2.1 shows the maximum deflection values measured and estimated by COMSOL for all membrane and magnet combinations. Also, experiment results for maximum deflections are illustrated in Figure 2.10. By setting the membrane relative permeability (μ_r) as 1.85, COMSOL simulations could estimate the experiment results for maximum deflection conditions with high performance (R^2 = 0.9843).

Table 2.1 : Measured and simulated maximum deflection values for all membrane and magnet combinations, R^2 = 0.9843.

Membrane diameter [mm]	Magnet diameter [mm]	Measured max. deflection [μm]	COMSOL max. deflection [μm]
3.77	3	301	325
3.77	4	293	272
4.55	3	393	401
4.55	4	371	382
5.73	3	511	495
5.73	4	514	507
6.83	3	564	568
6.83	4	597	602

The experiments which were done by changing the distance between the magnet and the membrane were also simulated by COMSOL Multiphysics with the previously determined parameters. Measurements and simulation results were compared. Graphs in Figure 2.11 display experimental data and COMSOL simulation results. It was found that a fine agreement between COMSOL simulations and measurements was observed for all membranes. COMSOL simulations could achieve a fine consistency with R^2 values of more than 0.95.

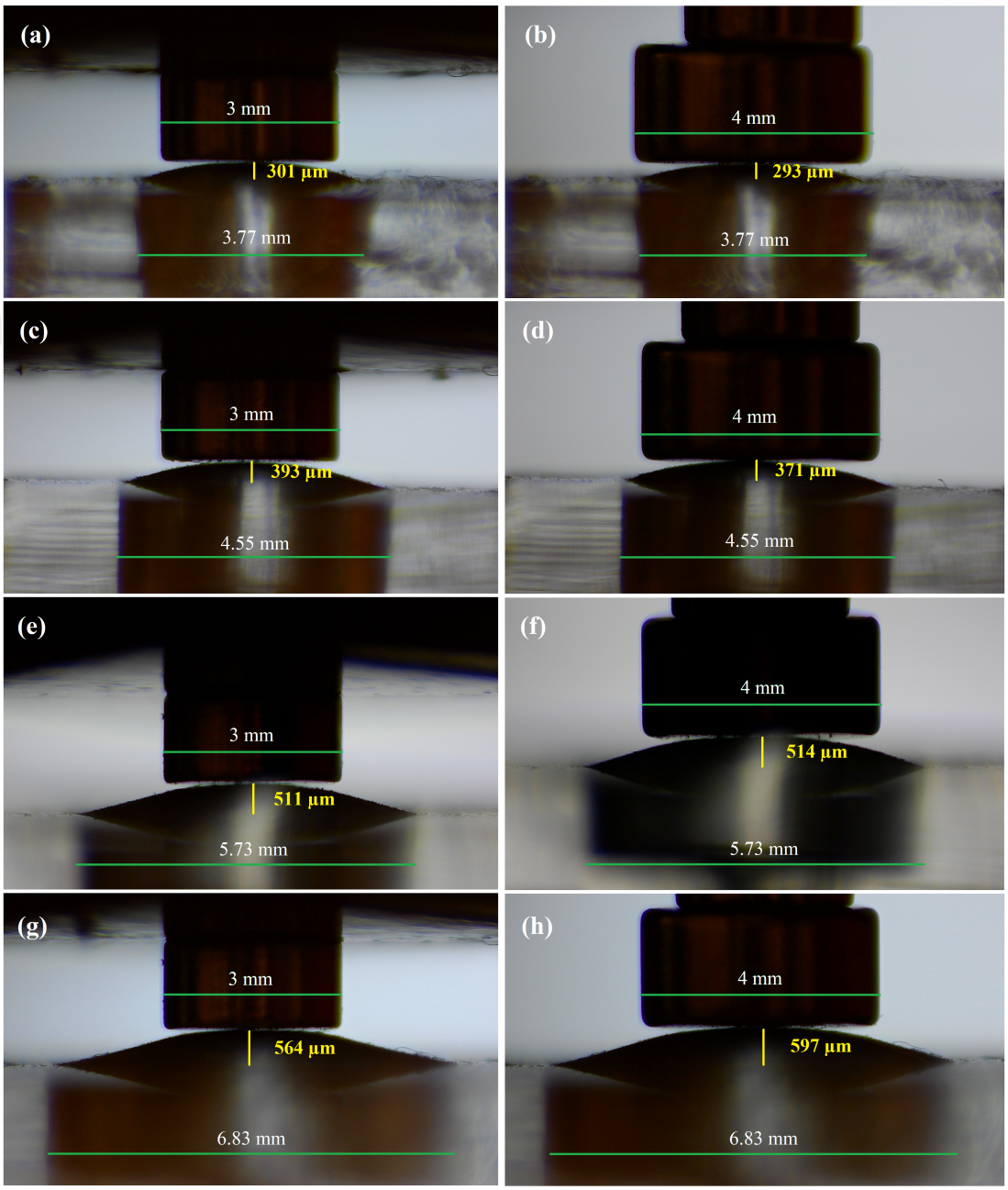

Figure 2.10 : Maximum deflection conditions for all membrane and magnet combinations.

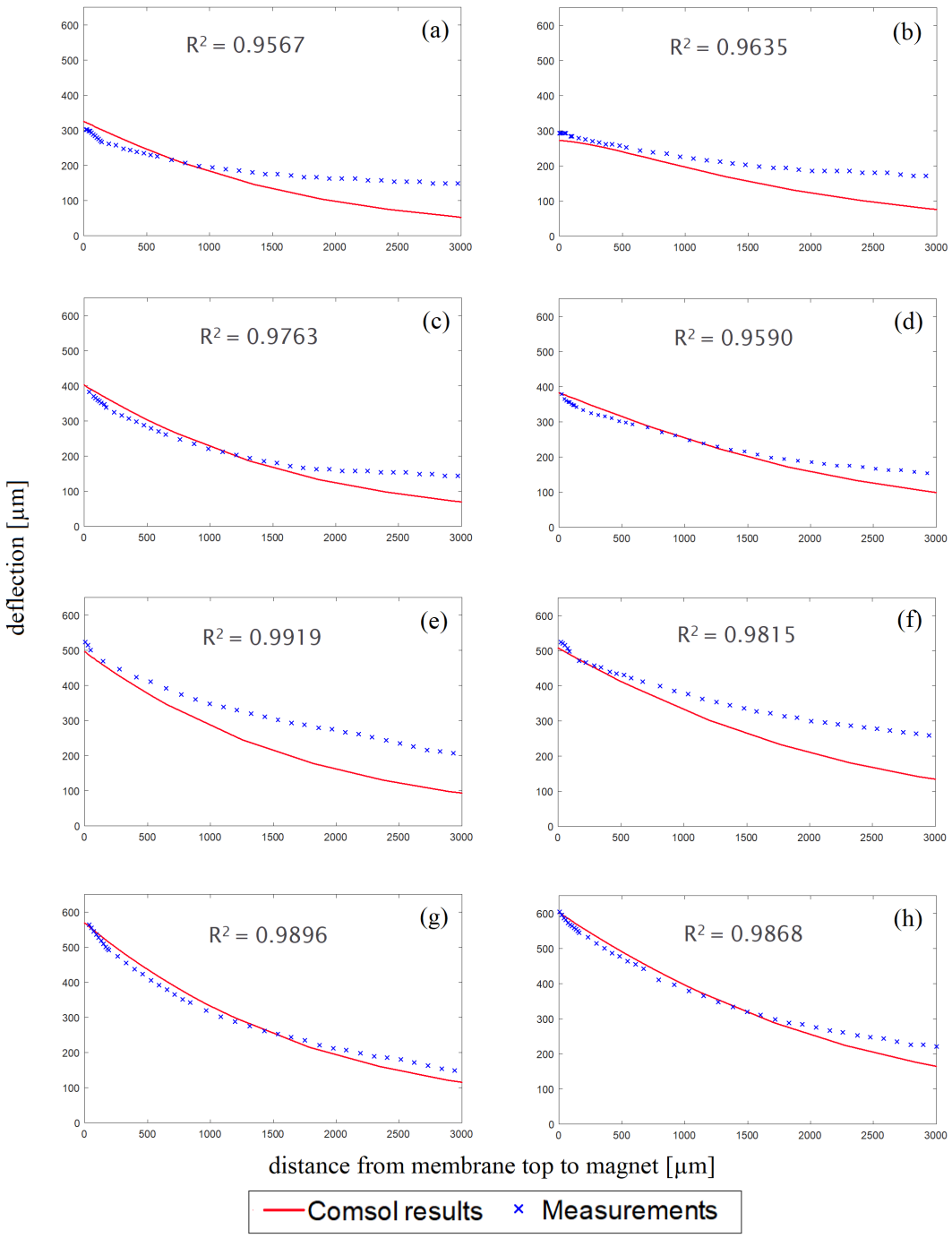

Figure 2.11 : Comparison of measured and simulated deflection values. a) 3 mm magnet - 3.77 mm membrane - $R^2 = 0.9567$, b) 4 mm magnet - 3.77 mm membrane - $R^2 = 0.9635$, c) 3 mm magnet - 4.55 mm membrane - $R^2 = 0.9763$, d) 4 mm magnet - 4.55 mm membrane - $R^2 = 0.9590$, e) 3 mm magnet - 5.73 mm membrane - $R^2 = 0.9919$, f) 4 mm magnet - 5.73 mm membrane - $R^2 = 0.9815$, g) 3 mm magnet - 6.83 mm membrane - $R^2 = 0.9896$, h) 4 mm magnet - 6.83 mm membrane - $R^2 = 0.9868$.

2.6 Discussion

In this study, CI-PDMS composite membranes were fabricated, tested, and simulated. Magnetic membranes having 30 μm thickness and different diameters were achieved with an easy fabrication process. No agglomeration was observed in the membrane cross-section. It was shown that the membranes can be deflected with only NdFeB magnets. The maximum deflection was recorded as 597 μm from the membrane with 6.83 mm diameter and the magnet with 4 mm diameter and 2 mm height. Deflection experiments were simulated with COMSOL Multiphysics with high consistency (with R^2 value exceeding 0.95). A novel estimation technique was successfully applied for the unknown mechanical and magnetic properties of the membrane which are required for the simulations.

3. MAGNETICALLY ACTUATED MICROFLUIDIC CELL SORTER

3.1 Overview

In Chapter 2, it was demonstrated that magnetic membranes can be used as an actuator in microfluidic applications. In this chapter, the design, mathematical modeling, fabrication, simulations, and tests of a microfluidic cell sorter which is actuated by magnetic membranes will be represented.

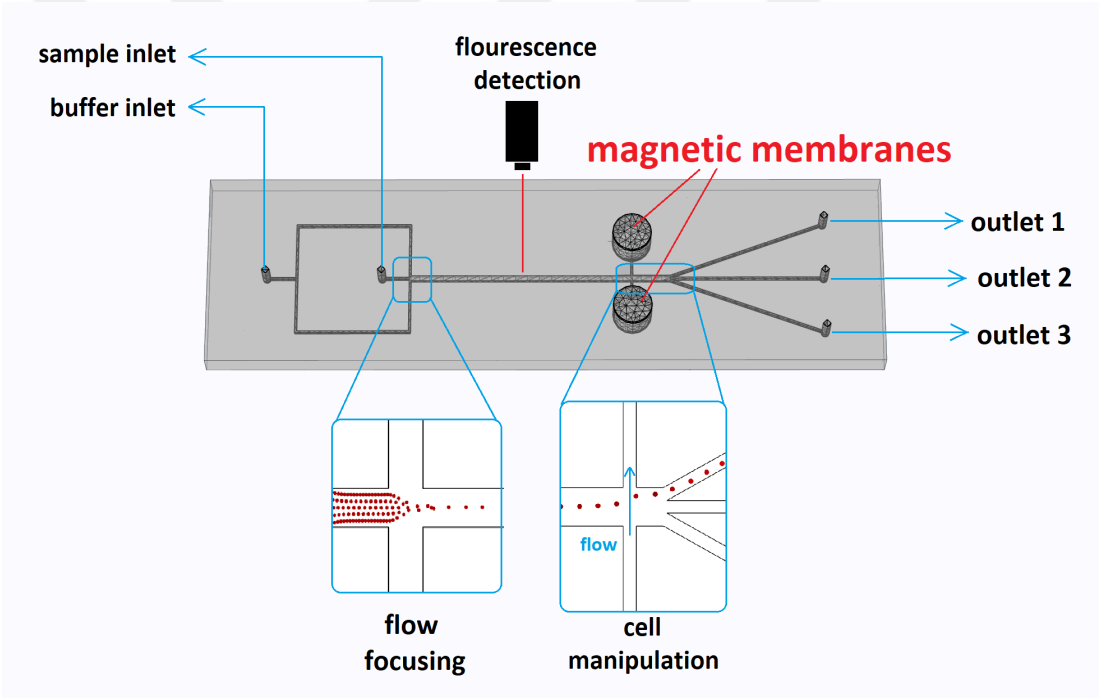

Figure 3.1 : Schematic diagram for our proposal magnetically actuated microfluidic cell sorter device.

The schematic diagram of our proposal device is illustrated in Figure 3.1. Sample solution and buffer solution are introduced to the chip from sample and buffer inlet respectively. The sample solution is squeezed by the buffer solution and cells are aligned in the flow focusing region. Then, cells are detected one by one by a camera system whether they are emitting fluorescence. According to the detection, the camera system trigger the magnetic membranes to manipulate the cells. Magnetic membranes, placed on both sides of the main channel, change the flow pattern in a perpendicular

direction to the mainstream by deflecting. Finally, cells flow out to the related outlet. There are three outlets on our device.

3.2 Materials and Methods

The device consists of three main parts: magnetic membrane, PDMS body, and glass bottom (Figure 3.2). Magnetic membrane and PDMS body are fabricated separately. Then, magnetic membrane, PDMS body, and glass bottom are assembled with oxygen plasma bonding.

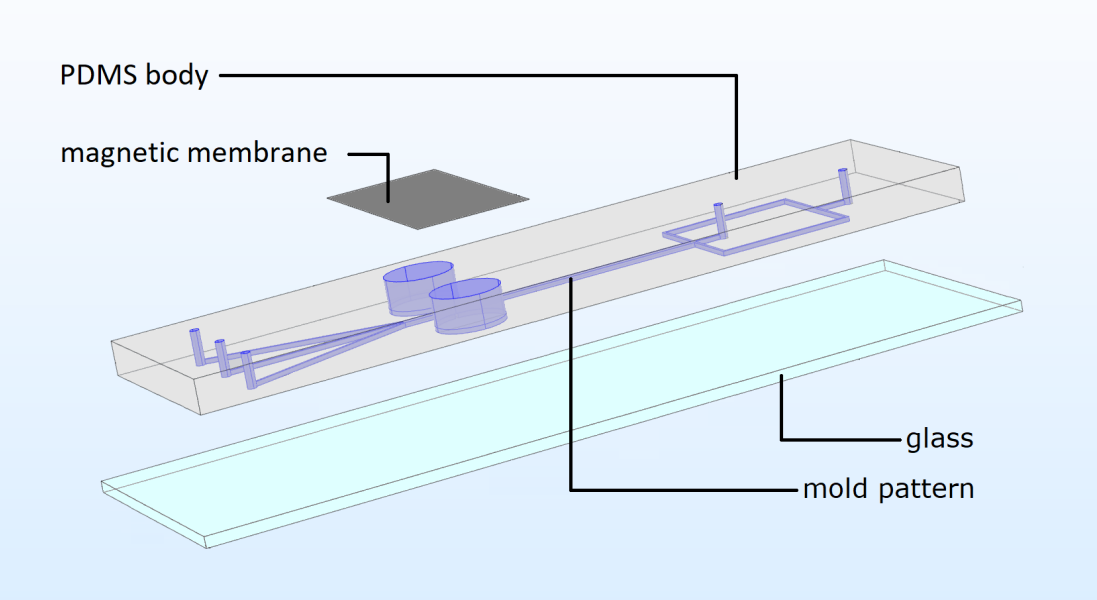

Figure 3.2 : Schematic diagram for our proposal magnetically actuated microfluidic cell sorter device.

Since the magnetic membrane fabrication was investigated in Chapter 2.3.1, PDMS body fabrication and magnetic actuator will be introduced in this chapter.

3.2.1 PDMS body fabrication

PDMS body fabrication starts with mold fabrication. The mold for the body was fabricated with kapton tape. The tape used for this study has 50 µm thickness. The 2D mold pattern was transferred to the tape using an electronic craft cutter (Silhouette Cameo). The mold pattern is given in Figure 3.3. In the figure, W_C is main channel width, D_M is membrane diameter, Wm is width of the channel between main channel and membranes, L_M is length of the channel between main channel. The total mold is slightly smaller than a microscope lame (25 mm x 75 mm). Also, the distance between

membrane centers is constant, 12 mm, so as that all chip can be actuated with the same magnetic actuator.

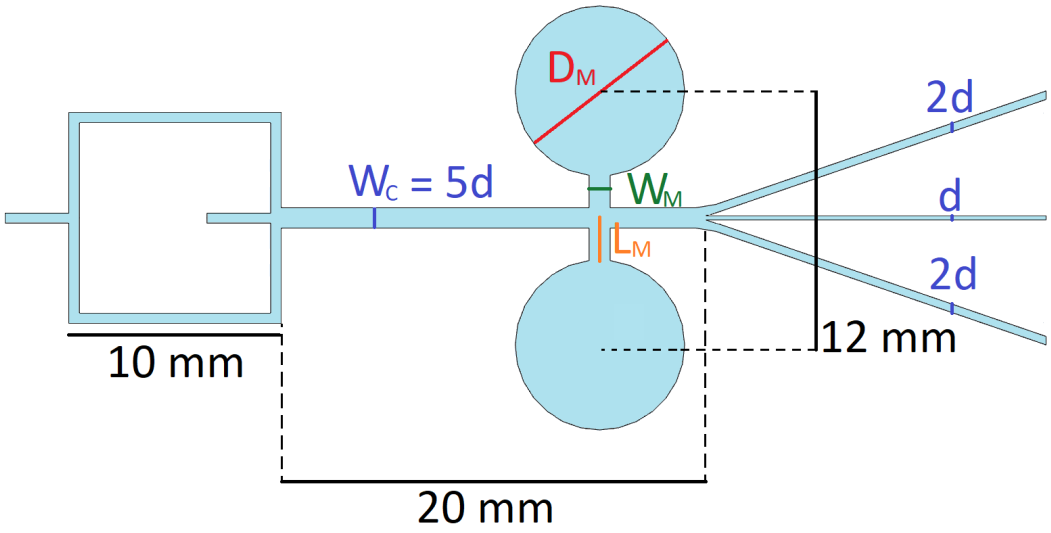

Figure 3.3 : 2D body mold draft.

To investigate the effects of dimensions four molds in different sizes were prepared. Table 3.1 gives the sizes of these molds. M_1, and M_2 have different W_M; M_1, and M_3 have different D_M, and L_M; M_2, and M_4 have different d and W_C.

Table 3.1 : Sizes of the molds fabricated. Each mold was fabricated to investigate the effect of the different parameter.

Mold name	d [µm]	W_C [µm]	D_M [mm]	L_M [mm]	W_M [mm]
M_1	200	1000	8	2	1.0
M_2	200	1000	8	2	0.5
M_3	200	1000	6	3	1.0
M_4	150	750	8	2	0.5

For mold fabrication, first, two layers of kapton tape was applied to one sheet of paper. Then, the top kapton tape layer was cut by the electronic craft cutter (Figure 3.4a). The bottom kapton tape layer was used as the bottom of the mold since it can be released from PDMS easily and the surface of the tape is smooth enough. Finally, the residual part of the top tape was peeled off (Figure 3.4b and c).

After mold fabrication, a PDMS mixture having 10:1 was prepared and poured over the mold. The PDMS body was baked for 4 h at 65 °C, then peeled off. Next, inlets, outlets, and membrane chambers were punched. Finally, magnetic membrane, PDMS body and a microscope lame were bonded with oxygen plasma treatment (Figure 3.5).

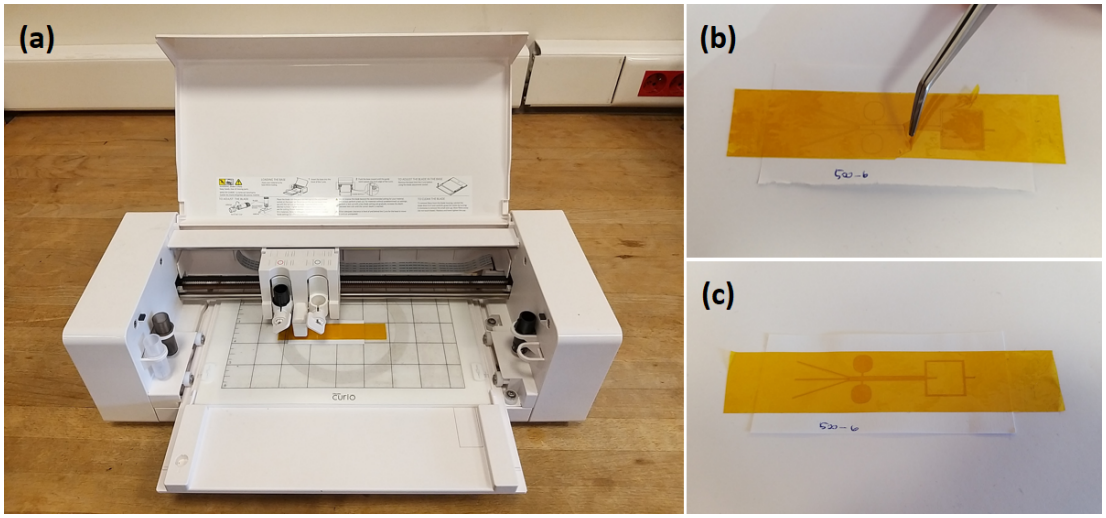

Figure 3.4 : Mold fabrication for PDMS body. a) Electronic craft cutter, b) peeling off the residual part with tweezers, c) final form of the mold.

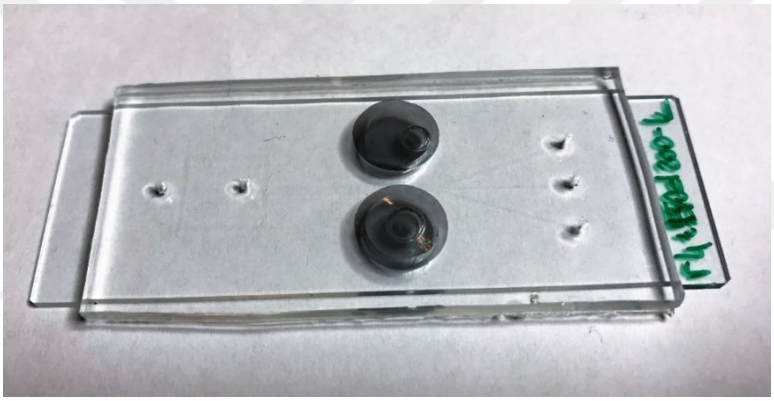

Figure 3.5 : Final form of the cell sorter chip

3.2.2 Magnetic actuator fabrication

In this study, the magnetic actuator was used to actuate the magnetic membranes. In previous chapter, it was demonstrated that magnetic membrane can be actuated by NdFeB magnets. Since the aim was to control the membranes electrically, magnets were controlled with inductors.

The magnetic actuator consists of four main parts: NdFeB magnets, inductors, a spring to hold magnets, and a platform to suspend the spring (Figure 3.6). For easy fabrication, the spring and the platform were fabricated with 3D printer.

First, two inductors (68.4 mH) were soldered to a board. Then, a rectangular wall was printed with PLA (poly lactic acid). After that, a spring was printed with TPU

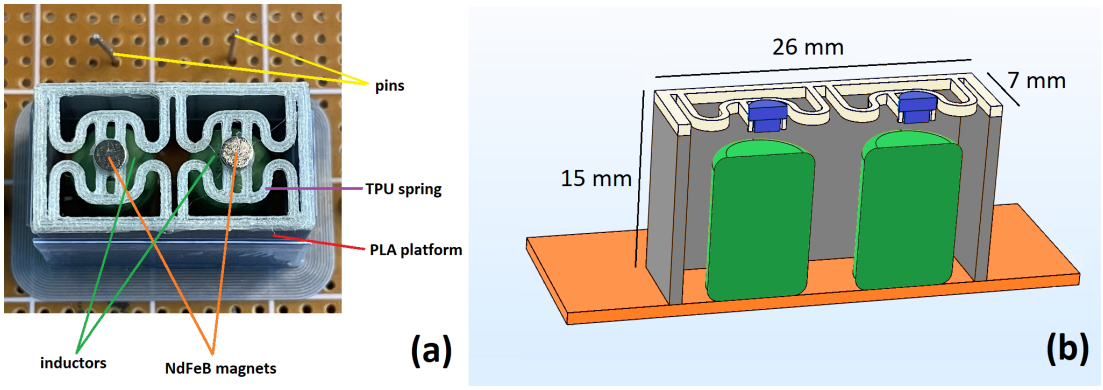

Figure 3.6 : Magnetic actuator. a) Real image, b) cross section of CAD image.

(thermoplastic poly urethane). TPU was preferred due to its flexibility. Finally, all parts were assembled with epoxy by aligning magnets, inductors, and spring.

3.2.3 Experiment setup

In cell sorter experiments, four different microfluidic cell sorter chips which are fabricated with M_1, M_2, M_3, and M_4 molds were tested by using dyed water as sample solution, and water as buffer solution. These solutions were pumped to inlets with syringe pump. At the same time, outlets were pumped with time same flow rate to make magnetic membranes in flat condition under atmospheric pressure. The deviation of the dyed water in cell manipulation area and outlets was observed with microscope by applying anti-phase square waves to inductors.

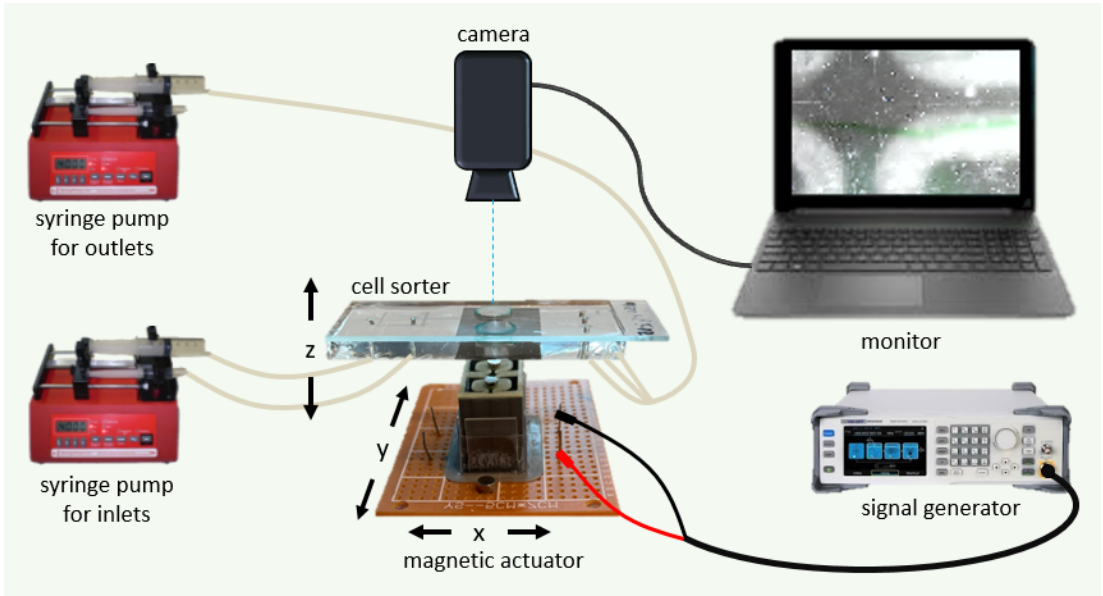

Figure 3.7 : Cell sorter experiment setup.

The experiment setup is shown in Figure 3.7. The chip and the actuator were held two translation stages; therefore, they can be moved laterally and vertically (in x and z direction). The camera was set to focus on the observation area. The voltage was applied to magnetic actuator with a signal generator.

Let's call the chips fabricated with M_1, M_2, M_3, and M_4 molds respectively C_1, C_2, C_3, and C_4. All these chips were tested for different inflow velocity, voltage, pulse width values. These values are given in Table 3.2. Maximum drift distances and response times were recorded based on the experiments.

Table 3.2 : Experiment parameters.

Experiment no	Inflow velocity [mm/s]	Voltage [V]	Pulse width [s]
E_1	6.4	0 - 10	0.2
E_2	12.8	0 - 10	0.2
E_3	19.2	0 - 10	0.2
E_4	6.4	8	0 - 0.5
E_5	12.8	8	0 - 0.5
E_6	19.2	8	0 - 0.5
E_7	6.4	10	20

For the preparation of the chips before experiments, first, the chips were placed in a water-filled container and filled with water in the desiccator with a vacuum pump. After the chips were completely filled with water, they were removed from the desiccator by keeping them in the water-filled container. Then, the inlet and outlet pipes were inserted to the chips. Green food dyed water and pure water were used as sample and buffer solutions respectively. Afterward, the chips were removed from the water-filled container and attached to the stages so that they were aligned with the magnets. Then, the camera was settled just above the chips and focused on the cell manipulation area.

Finally, the z-position of each chip was adjusted so that the maximum drift of the dyed water was equal to half of the main channel width. For different voltages and pulse widths, the deviation of dyed water was recorded for post image processing.

3.3 Mathematical Modeling

In this chapter, only the cell manipulation region of the cell sorter will be investigated since being the critical region in terms of sorting. Figure 3.8 illustrates this region.

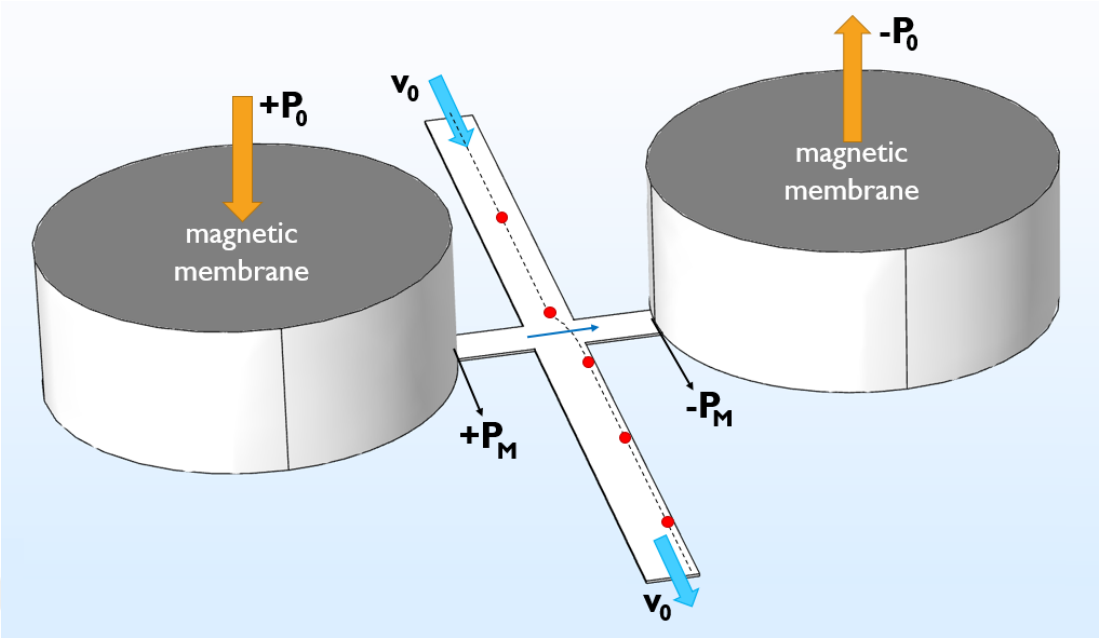

Figure 3.8 : Cell manipulation region of the chip. A particle is drifting to right when the right membrane is being pulled and the left one is being pushed.

In the figure, the right magnetic membrane is being pulled with P_0 pressure while the left one is being pushed. For this case, the pressure of the chamber entrances is defined as $+P_M$ and $-P_M$ for the left and right one respectively. The inflow and outflow velocity of the main channel is constant, v_0. In this condition, a cell enters to the main channel is drifted to right on the level of horizontal channel.

Now, it is necessary to analyze the flow in the horizontal channel more closely (Figure 3.9). In the figure, W_C is main channel width, H_C is channel height, W_M is width of the channel between main channel and membranes, L_M is length of the channel between main channel, v_x is lateral flow velocity [m/s], and Q_x is lateral volumetric flow rate [m^3/s]. Cells are drifted as much as they are exposed to the lateral flow between the positions 1 and 2.

Let's start with the lateral volumetric flow rate (Q_x) calculation. According to the Hagen-Poiseuille's Law (2.1) there is a linear relationship between pressure drop along the channel Δp [Pa], and the volumetric flow rate,

$$\Delta p = R_H \, Q \tag{3.1}$$

where R_H [Pa.s/m^3], is the hydraulic resistance of the channel. The pressure at the entrance of the left membrane chamber (P_M) equals P_0 when the pressure is applied to

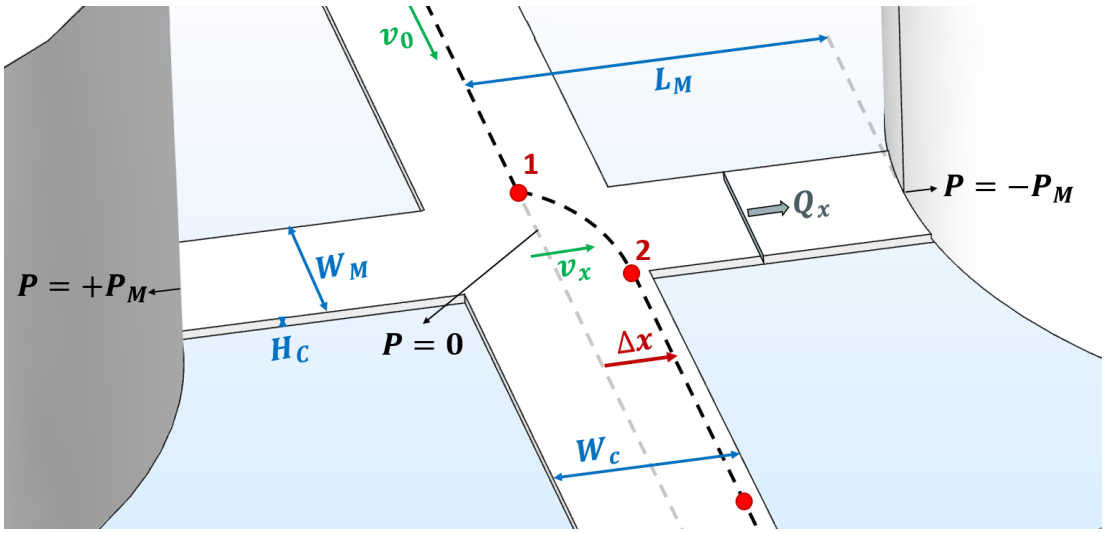

Figure 3.9 : Cell manipulation region, close view.

the membranes first, and it drops to 0 exponentially in time until the left chamber is filled fully. For the time constant of the system is τ, the pressure P_M can be written as in the following equation.

$$P_M(t) = P_0\, e^{-t/\tau} \tag{3.2}$$

Here, it can be assumed that the pressure on the center of the intersection zone of horizontal channel and main channel is zero by using the anti-symmetry in the channel. Therefore, the pressure drop from the center of the main channel to the entrance of the right chamber is:

$$\Delta p = 0 - \left(-P_M\right) = P_0\, e^{-t/\tau} \tag{3.3}$$

Now, R_H is required to calculate Q_x. By using hydraulic resistance equation for rectangular channels [46], R_H is defined as in equation (3.4).

$$R_H = \frac{12\,\eta\, L_M}{W_M\, H_C^3 \left(1 - 0.63\,\frac{H_C}{W_M}\right)} \tag{3.4}$$

Here, η is the liquid viscosity [Pa.s]. The lateral volumetric flow rate is calculated by using equation (3.1), (3.2), (3.3), and (3.4) as in the following equation:

$$Q_x(t) = \frac{P_0\, W_M\, H_C^3 \left(1 - 0.63\,\frac{H_C}{W_M}\right)}{12\,\eta\, L_M}\, e^{-t/\tau} \tag{3.5}$$

For $t = 0$, the lateral volumetric flow rate Q_{x0} is

$$Q_{x0}(t) = \frac{P_0\, W_M\, H_C^3 \left(1 - 0.63\,\frac{H_C}{W_M}\right)}{12\,\eta\, L_M} \tag{3.6}$$

Let's continue with τ calculation. In case of applying pressure to membranes for long enough time, the membranes are deflected maximum (w_0). In this case, the volume of the lateral flow should be equal to the volume change in the chambers, ΔV_M (3.7).

$$\Delta V_M = \int_{t=0}^{\infty} Q_x(t)\, dt = \frac{1}{2}\,\pi \left(\frac{D_M}{2}\right)^2 w_0 \tag{3.7}$$

Here, the volume change in the chambers is calculated with volume of paraboloid formula since the surface profile of the membranes will be parabolic [42]. Based on equation (3.7) and (2.1), the following equation is obtained for τ:

$$\tau = \frac{\Delta V_M}{Q_{x0}} = \frac{1.35\,\eta \left[\frac{\left(1-\nu_M^2\right)}{E_M\, d_M}\right]^{1/3} L_M\, D_M^{10/3}}{P_0^{2/3}\, W_M\, H_C^3 \left(1 - 0.63\,\frac{H_C}{W_M}\right)} \tag{3.8}$$

Finally, all the terms required for the drift distance of the cells (Δx) were obtained. Cells are drifted between the positions 1 and 2. If we define the times at these positions as t_1 and t_2, the drift duration Δt is equal to:

$$\Delta t = t_2 - t_1 = \frac{W_M}{v_0} \tag{3.9}$$

where W_M is the vertical distance and v_0 is the vertical flow velocity of the cells. And, the drift distance Δx is equal to:

$$\Delta x = \int_{t_1}^{t_2} v_x(t)\, dt \tag{3.10}$$

The flow profile is parabolic along the lateral channel, not uniform; therefore, $v_x(t)$ depends on not only time, but also the position. However, the average lateral flow velocity can substitute for $v_x(t)$. So, equation (3.10) can be written as following:

$$\Delta x = \int_{t_1}^{t_2} \frac{Q_x(t)}{H_C\, W_M}\, dt = \int_{t_1}^{t_2} \frac{Q_{x0}\, e^{-t/\tau}}{H_C\, W_M}\, dt \tag{3.11}$$

The solution of above equation can be analyzed for two extreme condition according to the Δt and τ values (3.12):

$$\Delta x = \frac{Q_{x0}\,\tau}{H_C\, W_M}\left(1 - e^{-\Delta t/\tau}\right) = \begin{cases} \dfrac{Q_{x0}\,\tau}{H_C\, W_M}, & \Delta t \gg \tau \\ \dfrac{Q_{x0}\,\Delta t}{H_C\, W_M}, & \Delta t \ll \tau \end{cases} \tag{3.12}$$

Since the sorting process takes place throughout drift, the sorting time of a cell equals to Δt. In this system, the aim is to drag the cell as fast as possible to change the cell's output. For short Δt, width of the horizontal channel can be decreased; however, it is limited by the production possibilities in the fabrication process. Also, the flow velocity of the main channel can be increased, and it is easy to set. In other words, for the short sorting time and high throughput, Δt is desired to be as little as possible, and it can be decreased easily by increasing v_0. So, the second case of equation (3.12) is valid.

To summaries, for 100% purity, throughput depends on v_0 and W_M (3.13).

$$throughput = \frac{v_0}{W_M} \tag{3.13}$$

Minimum W_M is limited by the resolution of fabrication techniques. But, throughput can increase with higher flow velocity. The drift distance Δx is (for $W_M \gg H_C$) given in the following equation by combining equation (3.6), (3.12), and (3.13).

$$\Delta x = \frac{P_0 H_C^2}{12\,\eta\, L_M} \frac{W_M}{v_0} = \frac{P_0 H_C^2}{12\,\eta\, L_M} \frac{1}{throughput} \tag{3.14}$$

For higher Δx, P_0 can be increased. In case magnet contacts membrane, P_0 depends on the magnetic properties of the magnet and the membrane, and the magnet diameter. However, the drift distance is not meaningful alone, because for narrower main channels, smaller drift is required. Therefore, the ratio of drift distance to main channel width is important here. To measure the sorting performance of the chip, the product of this ratio and throughput is calculated in equation (3.15).

$$\frac{\Delta x}{W_C} * throughput = \frac{P_0 H_C^2}{12\,\eta\, L_M W_C} \tag{3.15}$$

According to equation (3.15) the sorting performance increases with narrower main channel, and shorter membrane channel. But, the fabrication is limited by the electronic craft cutter resolution. Finally, H_C can be increased; however, it is also required for deeper chips to focus cells in z direction.

In our experiments, the effect of v_0, P_0, L_M, D_M, W_M, and W_C were tested.

3.4 Simulation

In this thesis, COMSOL Multiphysics 5.6a was used as finite element analysis of the cell sorter chips by utilizing Solid Mechanics, Laminar Flow, and Particle Tracing for Laminar Flow modules. To simplify the simulations only the cell manipulation region was simulated. The 3D geometry of the simulated part is shown in Figure 3.10.

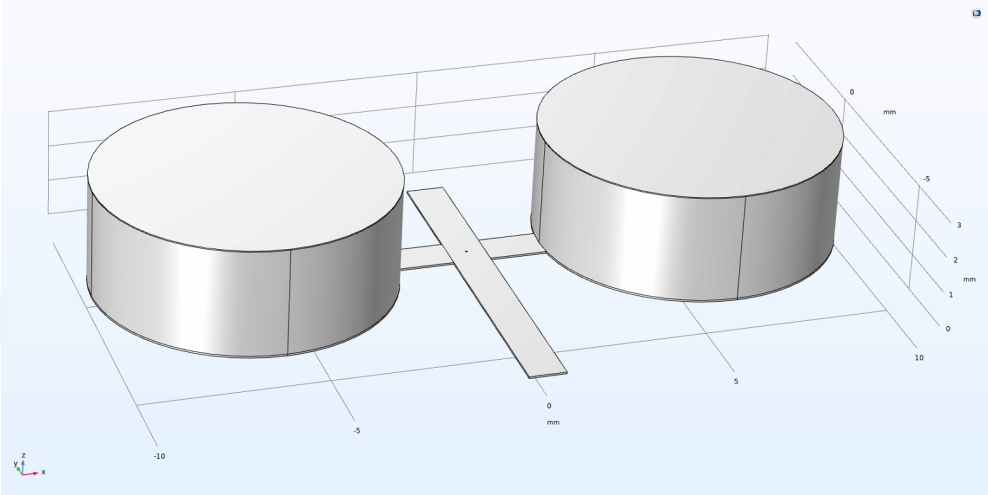

Figure 3.10 : COMSOL Multiphysics 3D geometry.

Simulations were run by changing mold geometry, inflow velocity, pressure value, and pulse width.

3.4.1 Modeling of magnetic membrane

The magnetic membranes were defined as hyperelastic material by utilizing the Solid Mechanics module. The lame parameter μ which is required to define the elasticity of membranes was set as 1.197 MPa, the same as the previous chapter.

For simplicity of the simulation, magnets were not defined separately. The force caused by magnets was defined as the boundary load applied to each membrane. Boundary loads are anti-phase pulses that have a maximum pressure of P_0 during the pulse width (Figure 3.11).

Finally, side edges of the membranes were fixed with Fixed Constraints.

3.4.2 Modeling of fluid flow

As the fluid inside the chip, water was selected. Normal inflow and outflow velocities were set as v_0 for the main channel. Also, the pressure was set to 0 at the intersection

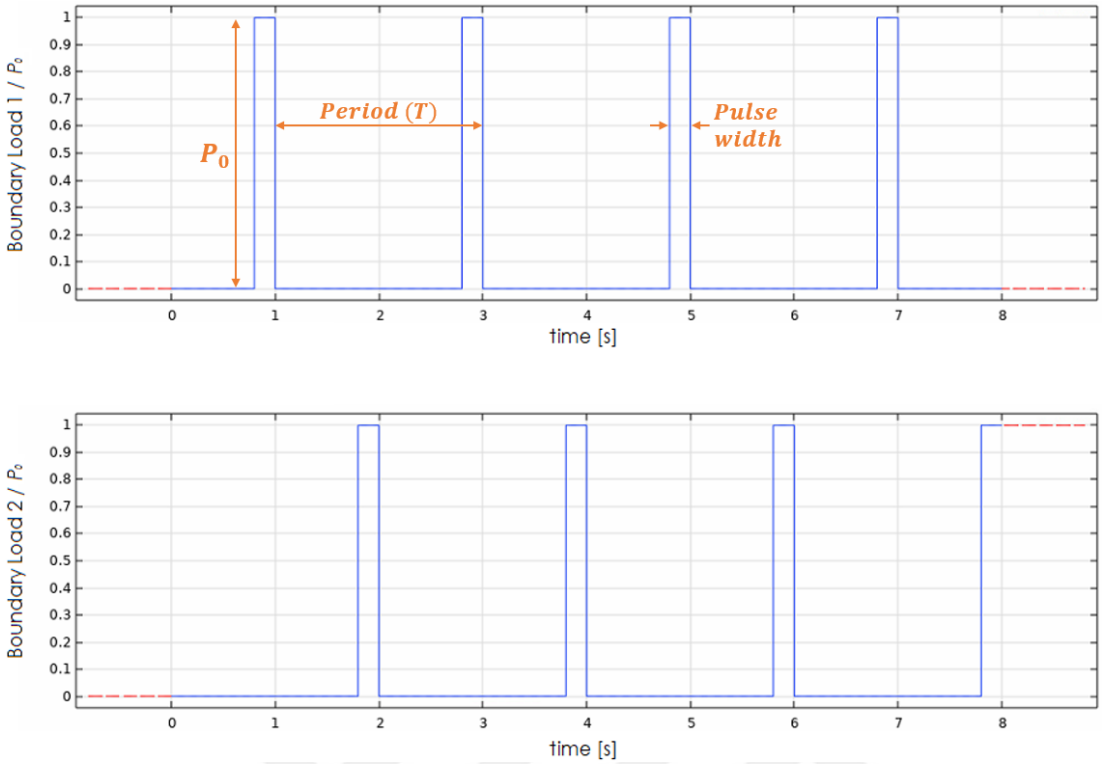

Figure 3.11 : Boundary loads for each membrane. Anti-phase pulses are applied to membranes.

of the main channel and the horizontal channel to ensure the pressure symmetry horizontally.

Since stream lines change with membrane actuation, a time-dependent study (Study 1) was computed for only Solid Mechanics and Laminar Flow modules to determine the streamlines.

3.4.3 Modeling of cells

Cells were defined as particles with Particle Tracing for Fluid Flow module. They were released from the center of the inlet surface.

To make the cells be transported by the fluid, a drag force was defined on the cells as the velocity field of the fluid.

Finally, a time-dependent study (Study 2) was computed for only Particle Tracing for Fluid Flow module to determine the horizontal drift distance (Δx) of the cells. As velocity field of the fluid flow, results of the first study was used.

3.5 Results

3.5.1 Mold fabrication review

First of all, the performance of the electronic craft cutter, Silhouette, has been investigated. 100, 200, 300, 400, 500, and 1000 µm wide stripes were drawn, then, cut with the cutter (Figure 3.12). The cutter was not able to produce the 100 µm wide stripe. According to the measurement of the width of the produced stripes, it has been inferred that the cutter is able to produce with an error rate lower than 10.0% after 500 µm (Table 3.3).

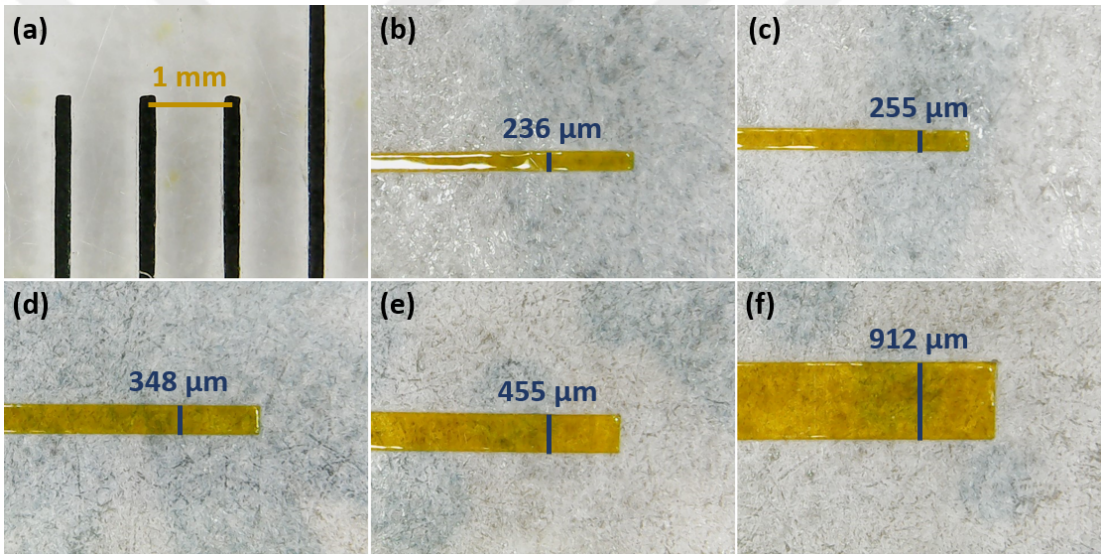

Figure 3.12 : Electronic craft cutter performance review, a) measurement reference ruler, b) 200 µm wide stripe, c) 300 µm wide stripe, d) 400 µm wide stripe, e) 500 µm wide stripe, f) 1000 µm wide stripe.

Table 3.3 : Electronic craft cutter performance review.

Drawn width [µm]	Measured width [µm]	Error rate [%]
200	236	18.0
300	255	15.0
400	348	13.0
500	455	9.0
1000	912	8.8

The mold fabricated are give in Figure 3.13. These molds were used 4 times and there is a visible damage to the molds. It has been observed that the tapes were lifted in

some parts, and breaking off some outlet legs of the molds. The chips were fabricated with damaged molds were not used for experiments.

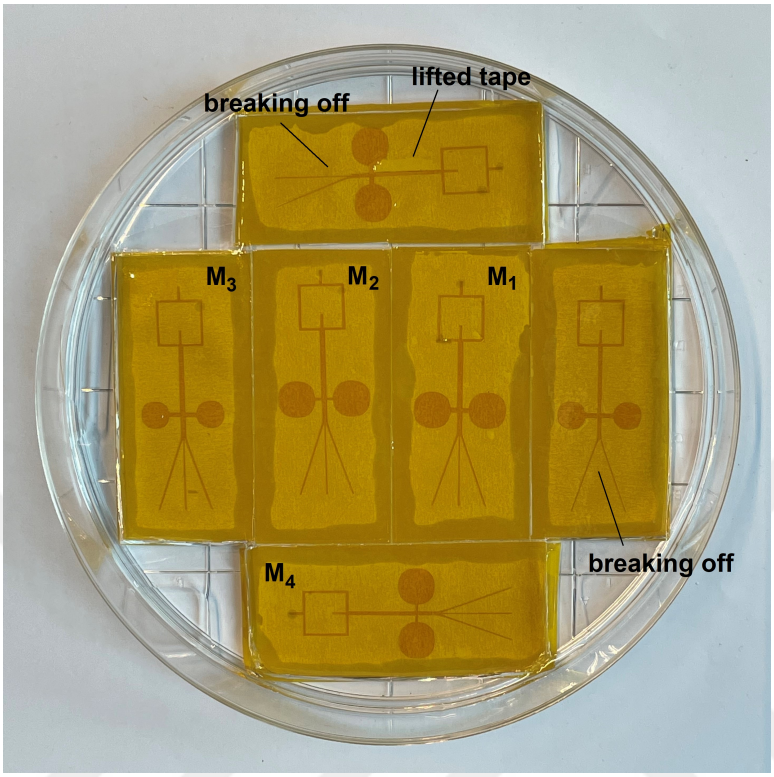

Figure 3.13 : Cell sorter molds. After 4 times uses, there was visible damage to the molds.

Additionally, the cell manipulation area and outlets of each mold were examined closely with a USB microscope (Figure 3.14). It has been observed that the sharp corners of all molds cannot be cut appropriately enough since the blade of the cutter has not good ability to turn. Moreover, it has been observed that outlet entrances of all molds are not sharp enough. Unfortunately, these areas are one of the most important parts of the molds that determine the chip performance and they should be perfect.

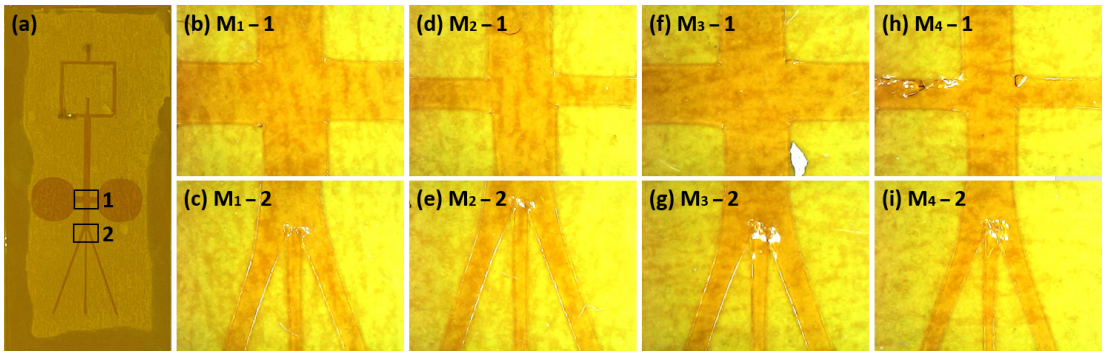

Figure 3.14 : Cell manipulation area and outlet entrances of each mold.

3.5.2 Theoretical results

The mathematical modeling of the chips has been done in Chapter 3.3. Based on this model, the effect of the inflow velocity (v_0) and pulse width of the applied voltage on the drift distance (Δx) has been analyzed for each chip (Figure 3.15). In the theoretical analysis, the maximum pressure (P_0) was settled the same as in the experiments so that the chips achieve maximum Δx for the minimum v_0.

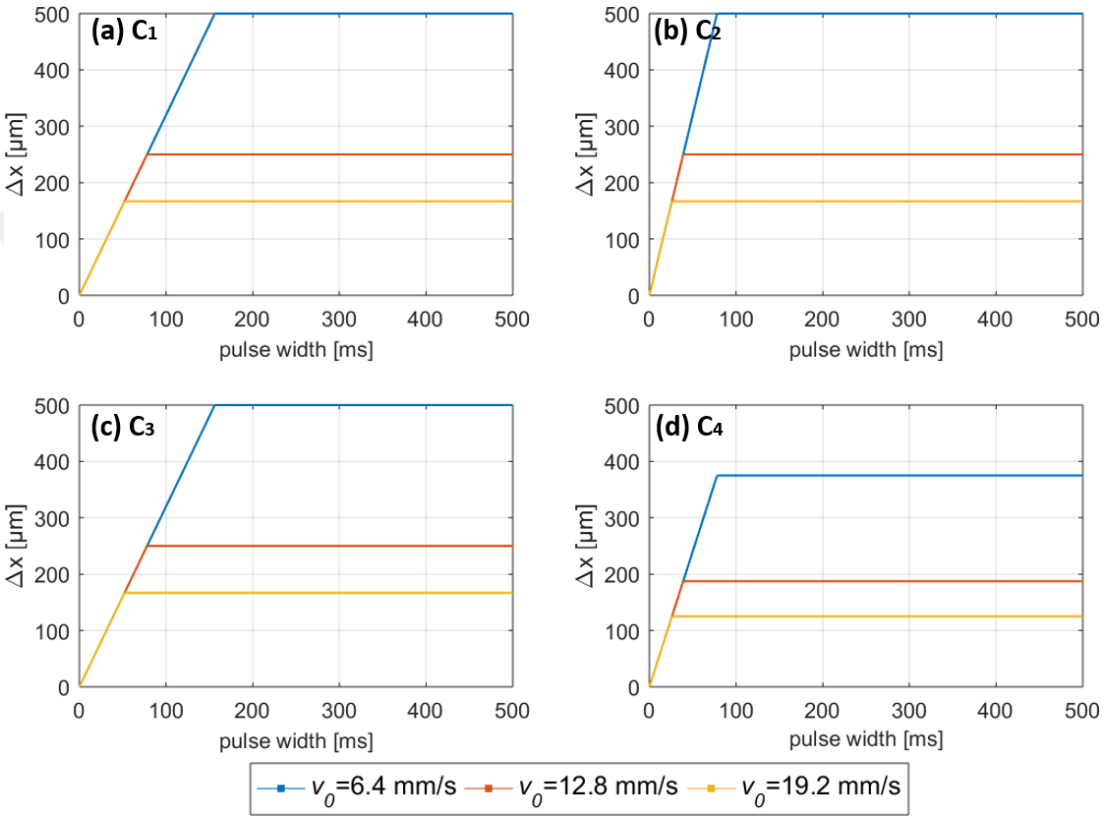

Figure 3.15 : The theoretical examination of the effect of the pulse width, and inflow velocity on the drift distance for each chip, a) C_1, b) C_2, c) C_3, d) C_4.

Figure 3.15 shows that the maximum drift distance (Δx) saturates after a certain pulse width. This certain value refers to the drift duration (Δt) for each chip. The C_1 and C_3 chips saturate later since their lateral channel widths are wider than others. So, it takes more time for cells to pass the cell manipulation area in these chips. Moreover, Δt decreases as v_0 increases since the cells pass the cell manipulation area more quickly. Up to the saturation, Δx increases linearly with the pulse width.

The graphs in Figure 3.15 additionally show that saturated Δx values are inversely proportional to v_0 because Δt decreases.

Finally, it can be inferred that chips have wider W_M reach the saturation later.

3.5.3 Simulation results

The COMSOL Multiphysics simulation of the chips has been defined in Chapter 3.4. After the studies were computed, Particle Trajectories results were analyzed to calculate the maximum drift distances (Figure 3.16).

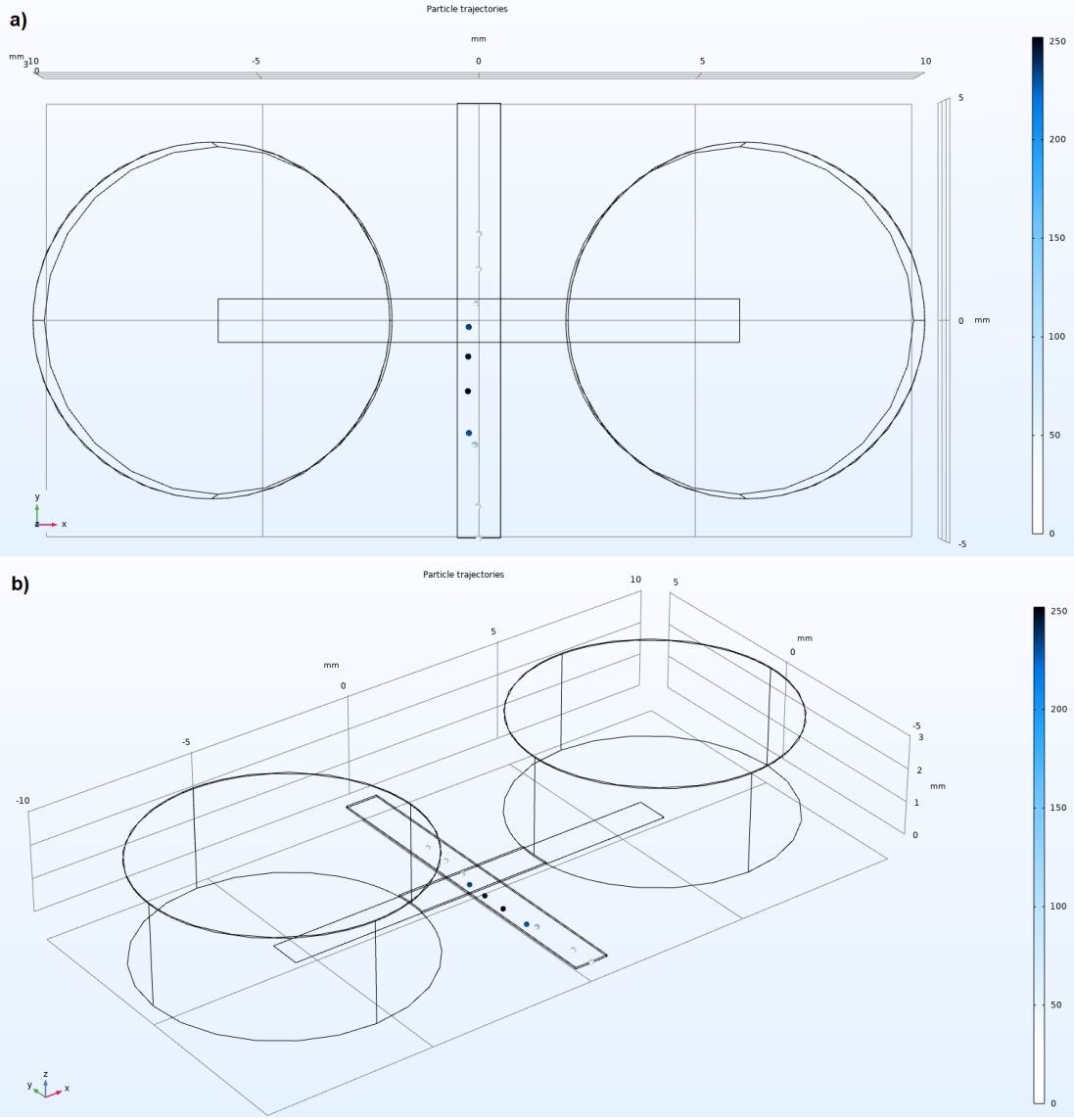

Figure 3.16 : a) 2D and b) 3D view of the Particle Trajectories results.

Based on the simulation model, the effect of the inflow velocity (v_0) and pulse width of the applied voltage on the drift distance (Δx) has been analyzed for each chip (Figure 3.17). In the model, the maximum pressure (P_0) was settled the same as in the experiments so that the chips achieve maximum Δx for the minimum v_0.

COMSOL simulation results have the same trends with the theoretical results. However, there is a small difference between them. COMSOL results reach saturation smoothly while the theoretical ones reach sharply. In the mathematical model, it has been assumed that the cell are exposed to the lateral flow only throughout the lateral channel and the lateral flow velocity is constant throughout the lateral channel. The difference comes from this assumption. On the other hand, the lateral flow becomes wider there in reality. Consequently, there is no sharp Δt value for saturation.

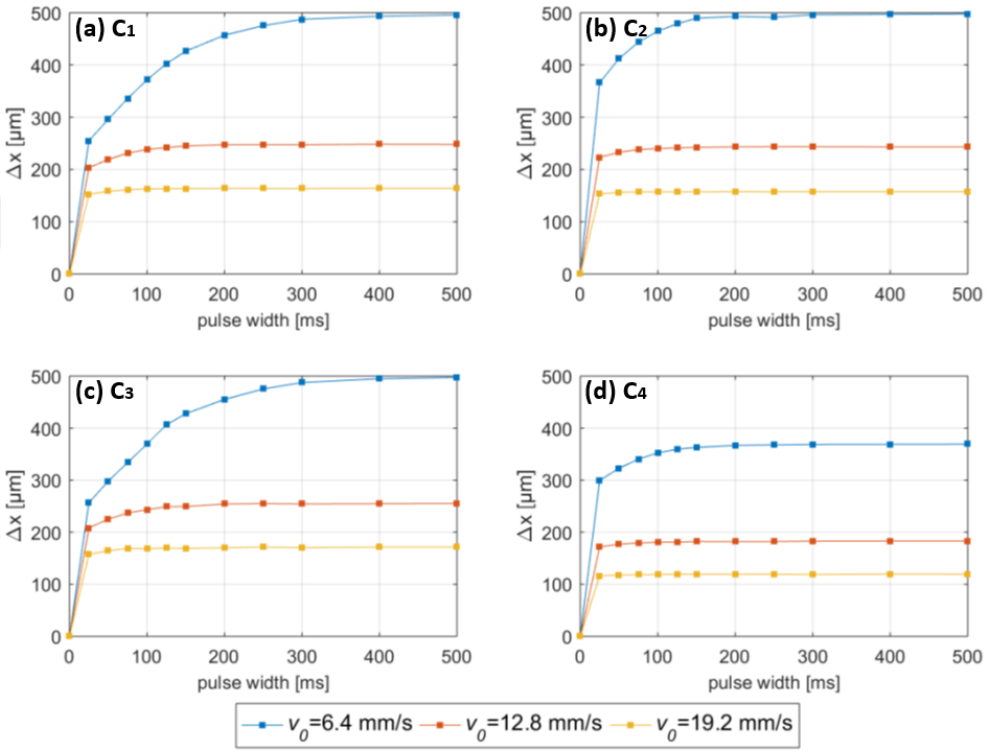

Figure 3.17 : The COMSOL Multiphysics examination of the effect of the pulse width, and inflow velocity on the drift distance for each chip, a) C_1, b) C_2, c) C_3, d) C_4.

3.5.4 Experiment results

Experiments were video-recorded and then the maximum drift distances were determined by applying color filter with ImageJ (Figure 3.18). The images captured from the video records have 640x480 pixels resolution. 1 pixel refers to 7.69 μm resolution.

Maximum drift distance (Δx) graphs of C_1, C_2, C_3, and C_4 chips for inflow velocity values of v_0 = 6.4, 12.8, and 19.2 mm/s, and voltages from 0 to 10 V are given in Figure 3.19.

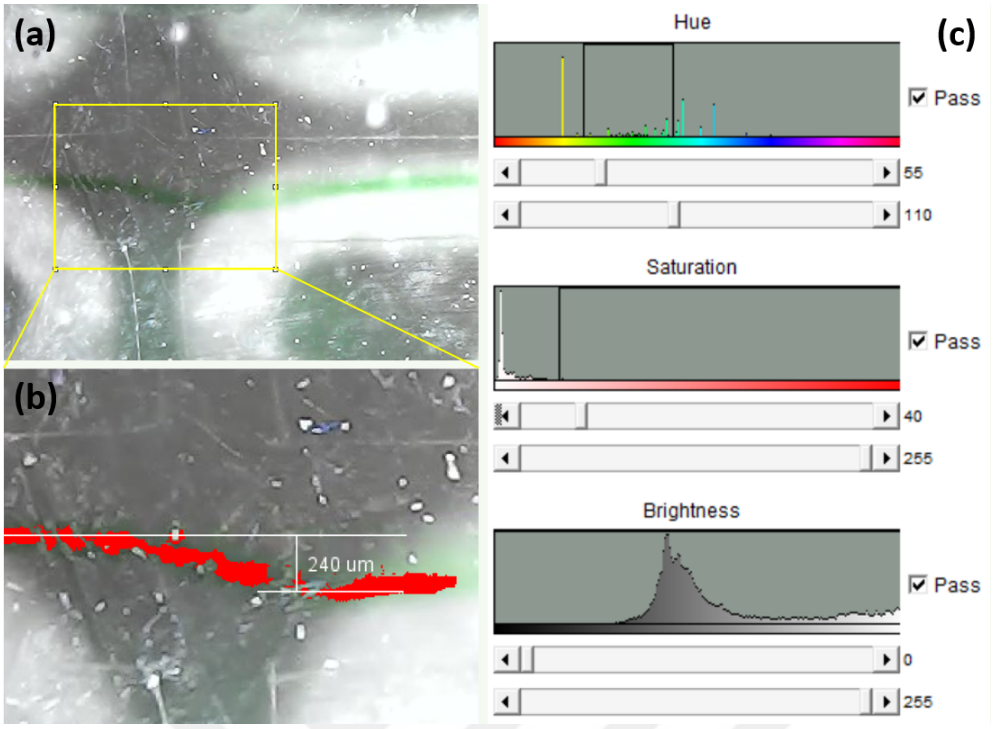

Figure 3.18 : Determination of the experiment results from video captures with ImageJ.

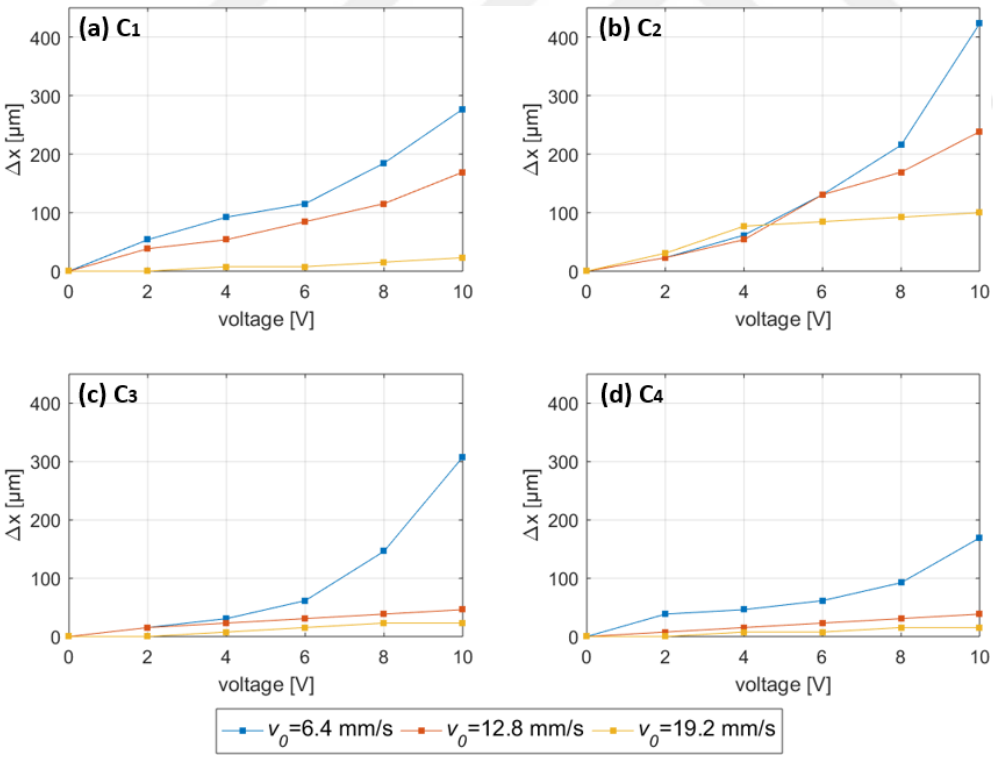

Figure 3.19 : The experimental examination of the effect of the voltage value, and inflow velocity on the drift distance for each chip, a) C_1, b) C_2, c) C_3, d) C_4.

As expected, increased drift distance has been observed for increasing voltage values and decreasing inflow velocity at each chip. The voltage required to direct the cell

flow from the middle output to the side output for the lowest inflow velocity was determined as 4, 6, 8, and 6 V for the C_1, C_2, C_3, and C_4 chips, respectively. That means, wider membrane actuators, and wider cell manipulation areas ease the cell deflection. This result is also consistent with theoretical calculations and COMSOL Multiphysics results.

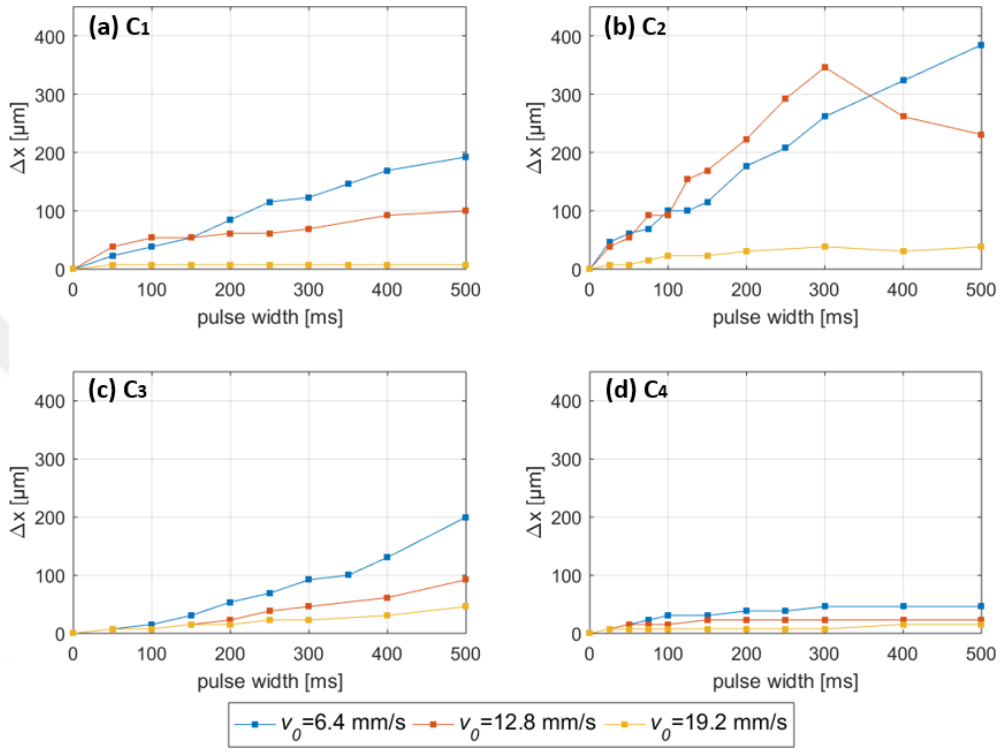

Figure 3.20 : The experimental examination of the effect of the pulse width, and inflow velocity on the drift distance for each chip, a) C_1, b) C_2, c) C_3, d) C_4.

Maximum drift distance (Δx) graphs of C_1, C_2, C_3, and C_4 chips for inflow velocity values of $v_0 = 6.4$, 12.8, and 19.2 mm/s, and pulse widths from 0 to 500 ms are given in Figure 3.20. According to theoretical calculations and COMSOL Multiphysics results, it was expected that the Δx would not increase after a certain pulse width (Δt). This pulse width is roughly equal to the time the cells are exposed to horizontal flow, and should increase as the width of the side channel (W_M) increases and the inflow velocity (v_0) decreases. The experimental results generally agree with this conclusion. However, as the pulse width increased, it was observed that the maximum deviation distance increased continuously, even if slightly.

Maximum drift distance (Δx) graphs of C_1, C_2, C_3, and C_4 chips for inflow velocity values of $v_0 = 6.4$ mm/s, and pulse widths from 0 to 200 s are given in Figure 3.18. The dots in the figure refer to the experimental measurements, and lines refer to the

exponentially fitted lines to these measurements. Response times of chips have been determined as 46.73, 9.10, 6.89, and 28.63 s in order. Response times are at the level of seconds which is extremely longer than Δt values.

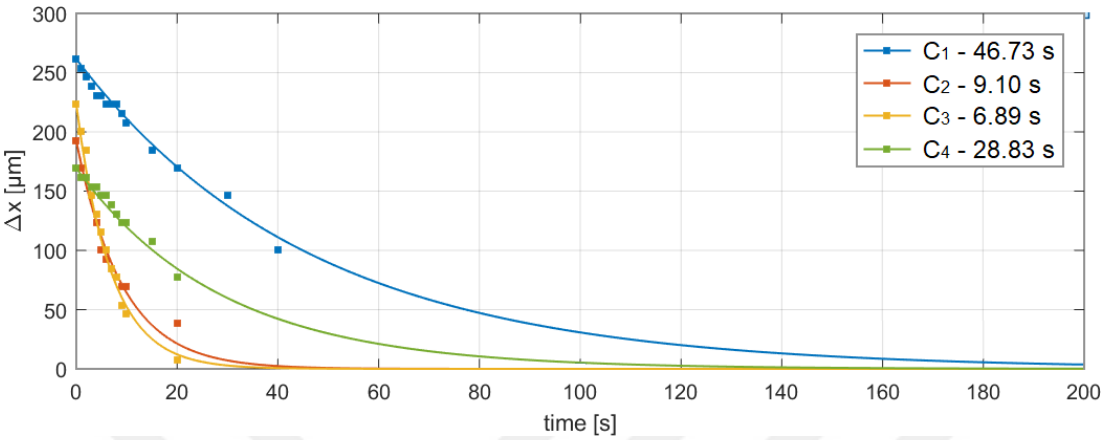

Figure 3.21 : Response time for each chip.

In addition, it has been observed that the results of experiments performed under the same conditions for the same chip are not consistent. It has been thought that this stems from the fact that the membranes were not completely flat in the initial state. Finally, the deviation of the flow from the middle outlet to the side outlet has not been observed as expected at any of the chips due to fabrication errors.

3.5.5 Design parameters examination

Finally, the chips have been compared to find the best chip design parameters. For comparison, theoretical results, simulation results, and experimental results of Experiment 4 (v_0 = 6.4 mm/s, pulse width = 0 - 500 ms) results have been analyzed.

To observe the effect of the lateral channel width (W_M) on the chip performance, C_1 and C_2 chips have been compared (Figure 3.22). C_1 has a wider main channel than C_2. Both theoretical, simulation, and experimental results shows that C_2 has a better performance. C_2 has a lower saturation time.

To observe the effect of the lateral channel length (L_M), and membrane radius (R_M) on the chip performance, C_1 and C_3 chips have been compared (Figure 3.23). C_1 has a wider membrane than C_3, and C_3 has a longer channel than C_1. Both theoretical, simulation, and experimental results shows that chips have almost similar performance.

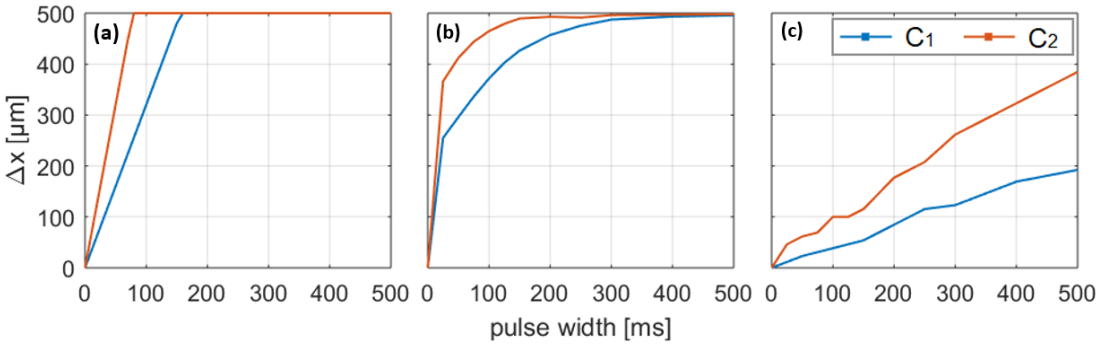

Figure 3.22 : Comparison of C_1 and C_2. a) Theoretical result, b) simulation result, c) experimental result. The effect of W_M has been analyzed.

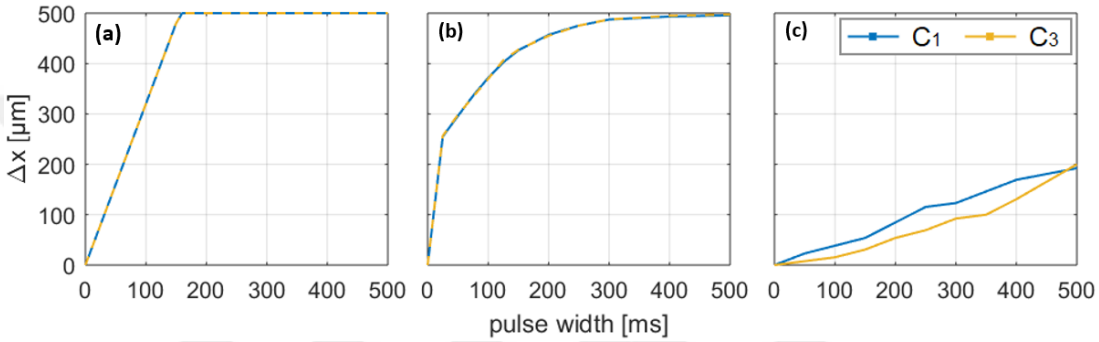

Figure 3.23 : Comparison of C_1 and C_3. a) Theoretical result, b) simulation result, c) experimental result. The effect of L_M and R_M has been analyzed.

To observe the effect of the main channel width (W_C) on the chip performance, C_2 and C_4 chips have been compared (Figure 3.24). C_2 has a wider main channel than C_4. Both theoretical, simulation, and experimental results shows that C_2 has a greater drift distance (Δx). However, it is not an important parameter because C_4 already requires a narrower Δx. On the other hand, C_4 has a lower saturation time based on the theoretical analysis, simulations, and experiments.

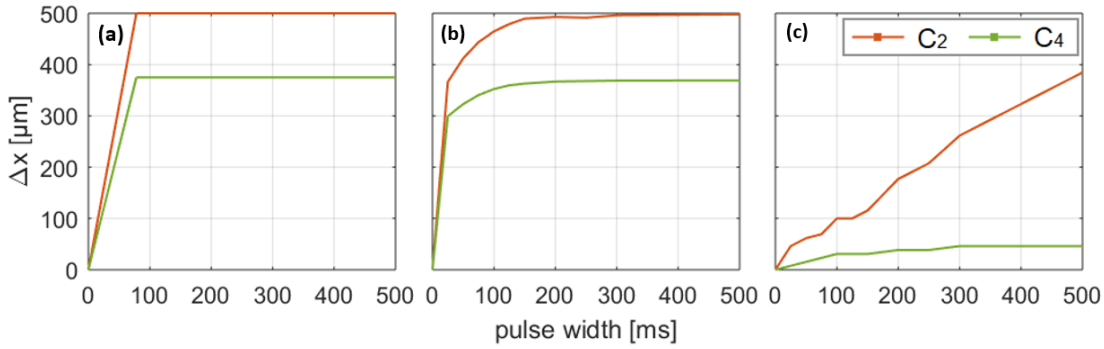

Figure 3.24 : Comparison of C_2 and C_4. a) Theoretical result, b) simulation result, c) experimental result. The effect of W_C has been analyzed.

Overall, both theoretical analysis, COMSOL Multiphysics results, and experiments shows that the best chip design should have a narrower W_M and W_C. Additionally, bigger membranes requires lower pulse amplitude (P_0) for actuation.

3.5.6 Chip outlets

The outlet entrances of each chip is shown in Figure 3.25. All of them have fabrication error. Because of these fabrication errors, any experiment can not be managed at the outlets.

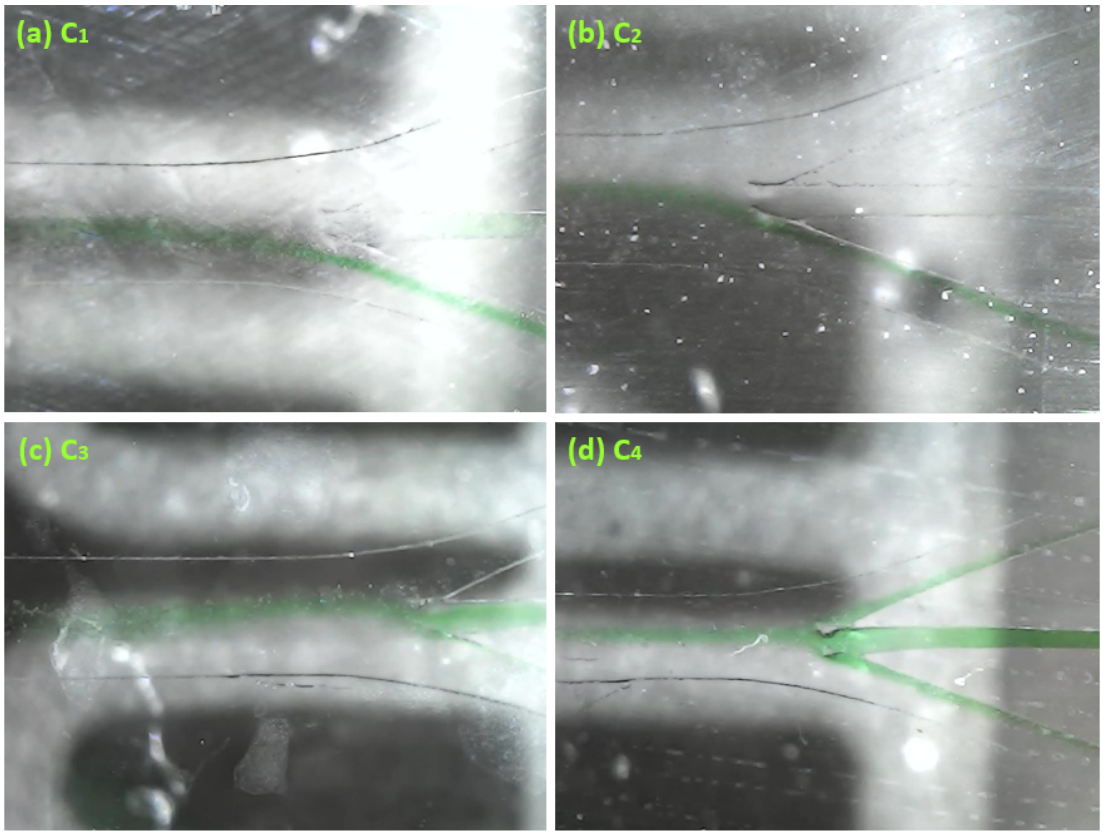

Figure 3.25 : The outlet entrances of each chip, a) C_1, b) C_2, c) C_3, d) C_4.

In the chips C_1 and C_2, the dyed water flows to bottom outlet although the flow was not manipulated in the main channel.In the chip C_3, the dyed water flows out to middle outlet although the flow was manipulated in the main channel. In the chip C_4, the dyed water flows to all outlets in all cases.

3.6 Discussion

In this study, a magnetically actuated cell sorter and its magnetic actuator were designed, fabricated, mathematically modeled, simulated, and tested.

The mold fabrication was done with electronic craft cutter which is a novel and practical technique. The electronic craft cutter was able to cut kapton tape with an error of less than 10% for sizes 500 μm and above. However, it was not successful enough in cutting sharp corners. In addition, the molds need to be renewed as they deform after a few uses.

The cell sorter chips with dimensions of 75 mm x 25 mm x 5 mm could be fabricated with a 5-6 hour process.

An electrically controllable magnetic actuator containing permanent magnets was fabricated with 3D printer to actuate the magnetic membranes. The magnetic actuators could operate the cell sorter with a voltage of 10 V and below.

The mathematically modeled of the cell sorter chip was done based on fundamental fluid mechanics. With this model, it was concluded that the chip size should be as small as possible and the liquid flow rate should be high in order to improve the chip performance.

The chips were simulated with the COMSOL Multiphysics 5.6a. Membranes, bio-fluid, and the cells were modeled with the Solid Mechanics, Laminar Flow, and Particle Tracing for Fluid Flow modules respectively. The simulation results were compatible with the mathematical model and experiments.

Finally, the chips were tested. Experiments were carried out by varying the amplitude of the applied voltage, pulse width and inflow velocity for the chips with different channel sizes. Experimental results were compatible with theoretical calculations and simulation results. However, when the experiments were repeated under the same conditions, the exact same results could not be obtained. This is thought to be due to the large size of the channels and the difficulty of setting the membranes completely flat in their initial state. Also, outlets of the chips could not be observed because of fabrication errors.

As a result, in this study, it has been achieved to produce a microfluidic cell sorter that can operate with 8 V voltage, have a throughput of 10 cells/s. The outputs of the chips could not be observed, as the outputs could not be cut properly enough with the electronic craft cutter. Only the deviation of the dyed water in the cell manipulation area could be observed.

4. CONCLUSION

In this thesis, a magnetically actuated cell sorter has been presented. The design, fabrication, simulation, mathematical modeling, and testing of the cell sorter have been thoroughly discussed. In addition, the design, fabrication, and simulation of the magnetic membranes and magnetic actuator which have been used as the actuation mechanism of the cell sorter have also been discussed. Novel and practical techniques for cell sorter mold fabrication, actuation mechanism of the cell sorter, magnetic membrane simulation, and electrically controllable magnetic actuator have been proposed and implemented successfully.

As a result, in this study, it has been achieved to produce a microfluidic cell sorter that can operate with 8 V voltage, have a throughput of 10 cells/s. It has been shown that it is possible to operate microfluidic cell sorters with magnetic membrane actuators. Unfortunately, a very low throughput has been achieved compared to other cell sorters in the literature. On the other hand, it has been proved with the theoretical calculations and simulation results that this cell sorter structure could rival those in the literature by fabricating in smaller sizes with advanced techniques.

As future works, it has been planning to manufacture the cell sorter in smaller sizes using more advanced techniques such as CNC machine, and test it with fluorescent activated beads.

REFERENCES

[1] **Lee, W.**, **Tseng, P. and Carlo, D.D.** (2016). Microfluidic Cell Sorting and Separation Technology, *Microsystems and Nanosystems Microtechnology for Cell Manipulation and Sorting*, 1–14.

[2] **Mattanovich, D. and Borth, N.** (2006). Review, Applications of cell sorting in biotechnology, *Microbial Cell Factories*, *5*(1), 12.

[3] **Kovarik, M.L.**, **Gach, P.C.**, **Ornoff, D.M.**, **Wang, Y.**, **Balowski, J.**, **Farrag, L. and Allbritton, N.** (2012). Micro Total Analysis Systems for Cell Biology and Biochemical Assays, *Analytical Chemistry*, *84*(2), 516–540.

[4] **Mckinnon, K.M.** (2018). Flow Cytometry: An Overview, *Current Protocols in Immunology*, *120*(1).

[5] **Gossett, D.R.**, **Weaver, W.M.**, **Mach, A.J.**, **Hur, S.C.**, **Tse, H.T.K.**, **Lee, W.**, **Amini, H. and Carlo, D.D.** (2010). Label-free cell separation and sorting in microfluidic systems, *Analytical and Bioanalytical Chemistry*, *397*(8), 3249–3267.

[6] **Al-Qudah, R. and Suen, C.Y.** (2021). Improving blood cells classification in peripheral blood smears using enhanced incremental training, *Computers in Biology and Medicine*, *131*, 104265.

[7] **Poudineh, M.**, **Labib, M.**, **Ahmed, S.**, **Nguyen, L.N.M.**, **Kermanshah, L.**, **Mohamadi, R.M.**, **Sargent, E.H. and Kelley, S.O.** (2016). Profiling Functional and Biochemical Phenotypes of Circulating Tumor Cells Using a Two-Dimensional Sorting Device, *Angewandte Chemie International Edition*, *56*(1), 163–168.

[8] **Iv, C.W.S.**, **Reyes, C.D. and López, G.P.** (2015). Microfluidic cell sorting: a review of the advances in the separation of cells from debulking to rare cell isolation, *Lab on a Chip*, *15*(5), 1230–1249.

[9] **Kye, H.G.**, **Park, B.S.**, **Lee, J.M.**, **Song, M.G.**, **Song, H.G.**, **Ahrberg, C.D. and Chung, B.G.** (2019). Dual-neodymium magnet-based microfluidic separation device, *Scientific Reports*, *9*(1).

[10] **Nitta, N. and et. al.** (2020). Raman image-activated cell sorting, *Nature Communications*, *11*(1).

[11] **Mutafopulos, K.**, **Spink, P.**, **Lofstrom, C.D.**, **Lu, P.J.**, **Lu, H.**, **Sharpe, J.C.**, **Franke, T. and Weitz, D.A.** (2019). Traveling surface acoustic wave (TSAW) microfluidic fluorescence activated cell sorter (μFACS), *Lab on a Chip*, *19*(14), 2435–2443.

[12] **Wong, I. and Ho, C.M.** (2009). Surface molecular property modifications for poly(dimethylsiloxane) (PDMS) based microfluidic devices, *Microfluidics and Nanofluidics*, *7*(3).

[13] **Mcdonald, J.C. and Whitesides, G.M.** (2002). Poly(dimethylsiloxane) as a Material for Fabricating Microfluidic Devices, *Accounts of Chemical Research*, *35*(7), 491–499.

[14] **Fiorini, G.S. and Chiu, D.T.** (2005). Disposable microfluidic devices: fabrication, function, and application, *BioTechniques*, *38*(3), 429–446.

[15] **Lee, W.**, **Tseng, P. and Carlo, D.D.** (2017). *Microtechnology for cell manipulation and sorting*, Springer International Publishing.

[16] **Bhagat, A.A.S.**, **Bow, H.**, **Hou, H.W.**, **Tan, S.J.**, **Han, J. and Lim, C.T.** (2010). Microfluidics for Cell Separation, *Medical Biological Engineering Computing*, *48*(10), 999–1014.

[17] **Karunanidhi, S.**, **Lum, M.W.**, **Nagurla, S.R. and Tang, W.C.** (2013). Microfluidic platforms for size-based cell sorting, *The 7th IEEE International Conference on Nano/Molecular Medicine and Engineering*.

[18] **Preira, P.**, **Grandné, V.**, **Forel, J.M.**, **Gabriele, S.**, **Camara, M. and Theodoly, O.** (2013). Passive circulating cell sorting by deformability using a microfluidic gradual filter, *Lab Chip*, *13*(1), 161–170.

[19] **Norouzi, N.**, **Bhakta, H.C. and Grover, W.H.** (2017). Sorting cells by their density, *Plos One*, *12*(7).

[20] **Zhang, J.**, **Yan, S.**, **Sluyter, R.**, **Li, W.**, **Alici, G. and Nguyen, N.T.** (2014). Inertial particle separation by differential equilibrium positions in a symmetrical serpentine micro-channel, *Scientific Reports*, *4*(1).

[21] **Yamada, M.**, **Nakashima, M. and Seki, M.** (2004). Pinched Flow Fractionation: Continuous Size Separation of Particles Utilizing a Laminar Flow Profile in a Pinched Microchannel, *Analytical Chemistry*, *76*(18), 5465–5471.

[22] **Mcgrath, J.**, **Jimenez, M. and Bridle, H.** (2014). Deterministic lateral displacement for particle separation: a review, *Lab Chip*, *14*(21), 4139–4158.

[23] **Choi, S.**, **Song, S.**, **Choi, C. and Park, J.K.** (2007). Continuous blood cell separation by hydrophoretic filtration, *Lab on a Chip*, *7*(11), 1532.

[24] **Cheng, Z.**, **Wu, X.**, **Cheng, J. and Liu, P.** (2017). Microfluidic fluorescence-activated cell sorting (μFACS) chip with integrated piezo-electric actuators for low-cost mammalian cell enrichment, *Microfluidics and Nanofluidics*, *21*(1).

[25] **Oh, S.**, **Jung, S.H.**, **Seo, H.**, **Min, M.K.**, **Kim, B.**, **Hahn, Y.K.**, **Kang, J.H. and Choi, S.** (2018). Magnetic activated cell sorting (MACS) pipette tip for immunomagnetic bacteria separation, *Sensors and Actuators B: Chemical*, *272*, 324–330.

[26] **Jiang, A.Y.L.**, **Yale, A.R.**, **Aghaamoo, M.**, **Lee, D.H.**, **Lee, A.P.**, **Adams, T.N.G. and Flanagan, L.A.** (2019). High-throughput continuous dielectrophoretic separation of neural stem cells, *Biomicrofluidics*, *13*(6), 064111.

[27] **Faridi, M.A.**, **Ramachandraiah, H.**, **Iranmanesh, I.**, **Grishenkov, D.**, **Wiklund, M. and Russom, A.** (2017). MicroBubble activated acoustic cell sorting, *Biomedical Microdevices*, *19*(2).

[28] **Yan, S.**, **Zhang, J.**, **Yuan, D. and Li, W.** (2016). Hybrid microfluidics combined with active and passive approaches for continuous cell separation, *Electrophoresis*, *38*(2), 238–249.

[29] **Sivaramakrishnan, M.**, **Kothandan, R.**, **Govindarajan, D.K.**, **Meganathan, Y. and Kandaswamy, K.** (2020). Active microfluidic systems for cell sorting and separation, *Current Opinion in Biomedical Engineering*, *13*, 60–68.

[30] **Ashcroft, R.G. and Lopez, P.A.** (2000). Commercial high speed machines open new opportunities in high throughput flow cytometry (HTFC), *Journal of Immunological Methods*, *243*(1-2), 13–24.

[31] **Cai, K.**, **Mankar, S.**, **Maslova, A.**, **Ajiri, T. and Yotoriyama, T.** (2020). Amplified piezoelectrically actuated on-chip flow switching for a rapid and stable microfluidic fluorescence activated cell sorter, *RSC Advances*, *10*(66), 40395–40405.

[32] **Ma, Z.**, **Zhou, Y.**, **Collins, D.J. and Ai, Y.** (2017). Fluorescence activated cell sorting via a focused traveling surface acoustic beam, *Lab on a Chip*, *17*(18), 3176–3185.

[33] **Wang, M.M.**, **Tu, E.**, **Raymond, D.E.**, **Yang, J.M.**, **Zhang, H.**, **Hagen, N.**, **Dees, B.**, **Mercer, E.M.**, **Forster, A.H.**, **Kariv, I. and et al.** (2005). Microfluidic sorting of mammalian cells by optical force switching, *Nature Biotechnology*, *23*(1), 83–87.

[34] **Meineke, G.**, **Hermans, M.**, **Klos, J.**, **Lenenbach, A. and Noll, R.** (2016). A microfluidic opto-caloric switch for sorting of particles by using 3D-hydrodynamic focusing based on SLE fabrication capabilities, *Lab on a Chip*, *16*(5), 820–828.

[35] **Pugliese, M.**, **Ferrara, F.**, **Bramanti, A.P.**, **Gigli, G. and Maiorano, V.** (2017). In-plane cost-effective magnetically actuated valve for microfluidic applications, *Smart Materials and Structures*, *26*(4), 045033.

[36] **Yu, H.**, **Zhou, G.**, **Chau, F.S. and Sinha, S.K.** (2011). Tunable electromagnetically actuated liquid-filled lens, *Sensors and Actuators A: Physical*, *167*(2), 602–607.

[37] **Tang, S.Q.**, **Li, K.H.H.**, **Yeo, Z.T.**, **Chan, W.X.**, **Tan, S.H.**, **Yoon, Y.J. and Ng, S.H.** (2018). Study of concentric, eccentric and split type magnetic membrane micro-mixers, *Sensing and Bio-Sensing Research*, *19*, 14–23.

[38] **Yamahata, C.**, **Lotto, C.**, **Al-Assaf, E. and Gijs, M.A.M.** (2004). A PMMA valveless micropump using electromagnetic actuation, *Microfluidics and Nanofluidics*, *1*(3), 197–207.

[39] **Said, M.M.**, **Yunas, J.**, **Pawinanto, R.E.**, **Majlis, B.Y. and Bais, B.** (2016). PDMS based electromagnetic actuator membrane with embedded magnetic particles in polymer composite, *Sensors and Actuators A: Physical*, *245*, 85–96.

[40] **Pirmoradi, F.**, **Cheng, L. and Chiao, M.** (2009). A magnetic poly(dimethylesiloxane) composite membrane incorporated with uniformly dispersed, coated iron oxide nanoparticles, *Journal of Micromechanics and Microengineering*, *20*(1), 015032.

[41] **Suna, A.**, **Gulle, M. and Erten, A.** (2019). Comparison of Magnetic Particle Incorporated PDMS Membrane Actuators, *2019 11th International Conference on Electrical and Electronics Engineering (ELECO)*.

[42] **Schomburg, W.K.** (2016). *Introduction to Microsystem Design*, Springer Berlin.

[43] **Park, B.J.**, **Fang, F.F.**, **Zhang, K. and Choi, H.J.** (2011). ChemInform Abstract: Polymer-Coated Magnetic Carbonyl Iron Microparticles and Their Magnetorheological Characteristics, *ChemInform*, *42*(16).

[44] **Wang, Z.**, **Volinsky, A.A. and Gallant, N.D.** (2014). Crosslinking effect on polydimethylsiloxane elastic modulus measured by custom-built compression instrument, *Journal of Applied Polymer Science*, *131*(22).

[45] **Li, J.**, **Zhang, M.**, **Wang, L.**, **Li, W.**, **Sheng, P. and Wen, W.** (2010). Design and fabrication of microfluidic mixer from carbonyl iron–PDMS composite membrane, *Microfluidics and Nanofluidics*, *10*(4), 919–925.

[46] **Araci, I.E.**, **Agaoglu, S.**, **Lee, J.Y.**, **Yepes, L.R.**, **Diep, P.**, **Martini, M. and Schmidt, A.** (2019). Flow stabilization in wearable microfluidic sensors enables noise suppression, *Lab on a Chip*, *19*(22), 3899–3908.

CURRICULUM VITAE

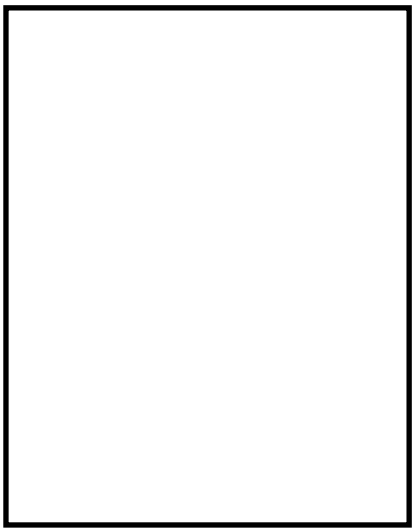

Name Surname: Merve Gülle

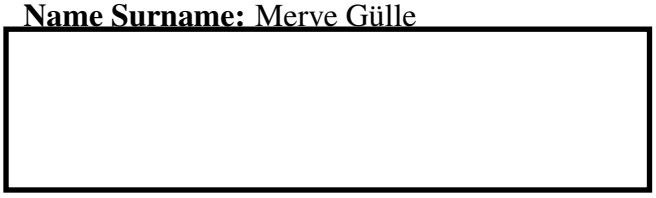

EDUCATION:

- **B.Sc.:** 2018, Istanbul Technical University, Faculty of Electrical and Electronics Engineering, Department of Electronics and Communications Engineering

PUBLICATIONS, PRESENTATIONS AND PATENTS ON THE THESIS:

- Suna A., Gulle M., Erten, A., 2019. Comparison of Magnetic Particle Incorporated PDMS Membrane Actuators, *11th International Conference on Electrical and Electronics Engineering (ELECO)*, November 28-30, 2019 Bursa, Turkey.